

Revised November 2021

(Typographical errors corrected and references updated August 13, 2022;

Fig. 8 corrected August 30, 2022)

First Submitted May 2021

# Numerical Techniques for Applications of Analytical Theories to Sequence-Dependent Phase Separations of Intrinsically Disordered Proteins

Yi-Hsuan LIN,<sup>1,2,†¶</sup> Jonas WESSÉN,<sup>1,†</sup> Tanmoy PAL,<sup>1,†</sup> Suman DAS,<sup>1</sup> and Hue Sun CHAN<sup>1,\*</sup>

<sup>1</sup>Department of Biochemistry, University of Toronto, Toronto, Ontario M5S 1A8, Canada;

<sup>2</sup>Molecular Medicine, Hospital for Sick Children, Toronto, Ontario M5G 0A4, Canada

† Contributed equally to this work.

¶ Present address: HTuO Biosciences Inc., Vancouver, B.C., Canada

\*Corresponding author

E-mail: huesun.chan@utoronto.ca; Tel: (416)978-2697; Fax: (416)978-8548

URL: <http://biochemistry.utoronto.ca/person/hue-sun-chan/>

Mailing address: Department of Biochemistry, University of Toronto, Medical Sciences Building – 5th Fl., 1 King’s College Circle, Toronto, Ontario M5S 1A8, Canada.

To appear as Chapter 3 in a *Methods in Molecular Biology* volume (~ October 2022) entitled “Phase-Separated Biomolecular Condensates”

*Edited by* Huan-Xiang Zhou, Jan-Hendrik Spille, and Priya Banerjee

Tentative page numbers of this chapter in the volume: pages 51–93

(hyperlinks to codes and related information are provided in the .pdf version of this preprint)

## Abstract

Biomolecular condensates, physically underpinned to a significant extent by liquid-liquid phase separation (LLPS), are now widely recognized by numerous experimental studies to be of fundamental biological, biomedical, and biophysical importance. In the face of experimental discoveries, analytical formulations emerged as a powerful yet tractable tool in recent theoretical investigations of the role of LLPS in the assembly and dissociation of these condensates. The pertinent LLPS often involves, though not exclusively, intrinsically disordered proteins engaging in multivalent interactions that are governed by their amino acid sequences. For researchers interested in applying these theoretical methods, here we provide a practical guide to a set of computational techniques devised for extracting sequence-dependent LLPS properties from analytical formulations. The numerical procedures covered include those for the determination of spinodal and binodal phase boundaries from a general free energy function with examples based on the random phase approximation in polymer theory, construction of tie lines for multiple-component LLPS, and field-theoretic simulation of multiple-chain heteropolymeric systems using complex Langevin dynamics. Since a more accurate physical picture often requires comparing analytical theory against explicit-chain model predictions, a commonly utilized methodology for coarse-grained molecular dynamics simulations of sequence-specific LLPS is also briefly outlined.

**Key words:** biomolecular condensates; membraneless organelles; intrinsically disordered proteins; polymer theory; Flory-Huggins theory; sequence charge pattern; random phase approximation; field-theoretical simulation; complex Langevin dynamics; coarse-grained molecular dynamics

# 1 Introduction

Biomolecular condensates in living organisms are functional microscopic compartments that, despite lacking a lipid-membrane boundary, maintain higher concentrations of specific sets of biomolecules within themselves compared with those of their surroundings [1]. Because of this defining feature, micron-sized intracellular biomolecular condensates are often referred to as membraneless organelles. A major physico-chemical driving force for the assembly of these condensates is the multivalent favorable interactions among biomolecules, resulting in liquid-liquid phase separation (LLPS), with higher concentrations of specific biomolecular species in the condensed phase [2, 3]. In this regard, a biomolecular condensate may be likened to a liquid droplet. The biomolecules involved can encompass intrinsically disordered proteins (IDPs), proteins containing both folded domains and intrinsically disordered regions (IDRs), globular proteins, and nucleic acids, or a subset thereof. As a versatile form of spatio-temporal organization of biochemical processes through the microenvironments they create, biomolecular condensates serve critical physiological functions. Accordingly, their dysfunction or misregulation can lead to disease (reviewed, e.g., in refs. [4, 5]). While functional intracellular biomolecular condensates can contain hundreds of biomolecular species organized in an extremely complex [6], out-of-equilibrium [7] manner, recent experimental advances indicate that a wealth of information on the biophysical properties and biological functions of biomolecular condensates can already be gleaned from equilibrium phase behaviors of highly simplified cell-free model systems consisting of one or only a few key biomolecular species as in the cases of FUS [8] and Ddx4 [9]. Therefore, it stands to reason that fundamental physical insights into how properties of biomolecular condensates are determined by the amino acid sequences of their major components, i.e., how molecular recognition leading to the assembly of biomolecular condensates is effectuated, can be gained by computational modeling and theoretical considerations of simplified heteropolymeric LLPS systems [10, 11].

## 1.1 Theoretical constructs at different levels of realism

With this perspective in mind, this chapter focuses primarily on analytical theories for sequence-dependent IDP/IDR LLPS. Analytical theories and computational models of heteropolymer LLPS may be constructed at different levels of structural and energetic realism [10], with a general trade-off between realism and computational efficiency. At one extreme, polymer LLPS can be described at a basic, mean-field level by Flory-Huggins (FH) theory [12] for polymers with spatially short range, contact-like interactions and Overbeek-Voorn (OV) theory [13] for polymers with spatially long range Coulomb interactions. The formalism of these theories are simple and the necessary numerical calculations for determining their predicted LLPS properties are straightforward. However, for IDP/IDR LLPS, while FH and OV theories account approximately for effects of sequence composition (the numbers of different types of amino acid residues in the IDP/IDR sequence), fundamentally

FH and OV are not equipped to fully account for sequence dependence because they make no distinction between sequences that share the same amino acid composition.

At the other extreme, simulations of atomistic IDP/IDR models using an explicit representation of water molecules should offer a much more realistic picture of LLPS enriched with structural and energetic details [14]; but the computational efficiency of atomistic modeling of IDP/IDR LLPS is a major current challenge because it requires simulating a large number of protein chains. Recent advances in this direction include an explicit-water, atomistic molecular dynamics study of IDP condensed-phase properties that relies and is built upon an initial implicit-solvent coarse-grained chain simulation for achieving equilibrium LLPS of the model system [15]. Because of the high computational cost of explicit-water atomic simulation, the number of LLPS systems that the research community can afford to examine by a fully atomistic approach would likely remain quite limited in the foreseeable future.

## 1.2 Random phase approximation in polymer theory

In this context, analytical theories and computational models that embody intermediate realism yet offer a higher degree of computational tractability are valuable for basic conceptual advances because they allow for efficient exploration of extensive arrays of possible physical scenarios. One of such approaches is the random phase approximation (RPA) in polymer theory, which goes beyond mean-field theories such as the FH and OV formalisms, which neglect fluctuations of polymer concentration, by an approximate account that takes into consideration the lowest-order concentration fluctuations [16]. The most significant progress enabled by RPA theories is their ability to account approximately for sequence dependence, as exemplified by the first theoretical account [17, 18] of the substantial difference in experimentally observed LLPS propensity between wildtype and a charge scrambled variant of Ddx4 IDR that share the same amino acid composition [9].

RPA theories of sequence-dependent LLPS and related theoretical developments were instrumental in uncovering [19] and elucidating [20] the relationship between isolated single-chain IDP properties [19] or binding affinity of a pair of IDPs [20] on one hand and multiple-chain LLPS propensity on the other [19–21]. An application of RPA to the LLPS of systems with two IDP species first indicated that their populations in the condensed phase are miscible when the sequence charge patterns [22, 23] of the two IDP species are similar, but they tend to demix into subcompartments when their sequence charge patterns are significantly different [24]. The robustness of this prediction has since been buttressed by explicit-chain coarse-grained molecular dynamics as well as field-theoretic simulations [25]. This finding highlights a stochastic, “fuzzy” type of molecular recognition that may contribute to subcompartmentalization of some biomolecular condensates [24] such as the nucleolus. The FIB1 and NPM1 IDPs that demix in the condensed phase of a simple cell-free model experimental system for the nucleolus [26] do have very different sequence charge patterns [24], although in-cell subcompartmentalization of the nucleolus likely involves much

more complicated, non-equilibrium mechanisms [27]. More recently, the development of an improved version of RPA with Kuhn length renormalization—referred to as rG-RPA—has further extended the applicability of RPA theories of sequence-dependent LLPS beyond that of neutral or near-neutral polyampholytes to include strongly charged polyelectrolytes as well [28].

Comparisons between predictions from analytical RPA theories and results from simulations of more realistic coarse-grained chain models conducted thus far indicate that the general trend of sequence dependence stipulated by the two approaches to modeling LLPS are consistent, but RPA tends to predict higher LLPS propensities than those predicted by coarse-grained explicit-chain models [29, 30]. This limitation of RPA, which is likely caused in large measure by its highly idealized treatment of chain excluded volume, should be borne in mind when RPA predictions are interpreted vis-à-vis experimental data or results from molecular dynamics simulations.

### 1.3 Polymer field-theoretic simulation

A more accurate—though computationally more intensive—method to extract observable consequences from typical polymer-theory Hamiltonians (energy functions) is field-theoretic simulation (FTS) [31–33]. Unlike RPA which accounts only for the lowest order of concentration fluctuations, in principle FTS is capable of accounting for concentration fluctuations in their entirety, though FTS is limited nonetheless by the necessary discretization and finite size of the simulation system. A comparison of FTS and RPA results on sequence-dependent polyampholyte LLPS indicates reassuringly that they are largely consistent except RPA is seen to be inaccurate, as expected, for a relatively small concentration regime where polymer is very dilute in solution [32].

FTS has been applied to compute correlation functions for systems with two IDP species. The results indicate that sequence charge-pattern mismatch and a strong generic excluded volume repulsion are both necessary for two polyampholytic IDP species to demix, i.e., to subcompartmentalize, in the condensed phase [25]. This conclusion is in line with the aforementioned RPA prediction with regard to sequence charge pattern mismatch because a strong excluded volume was tacitly enforced in that prior formulation by an incompressibility constraint [24]. The finding underscores the sensitivity of FTS predictions to excluded-volume assumptions, urging caution in choosing and interpreting FTS parameters for excluded volume [25]. Insofar as electrostatic effects in polyampholyte LLPS are concerned, recent studies using FTS, RPA, and coarse-grained explicit-chain molecular dynamics of polyampholytes with a simplified explicit model of polar solvent suggest that a reduced relative permittivity contributed by the solvent in the condensed phase probably leads only to a small to moderate enhancement of LLPS propensity compared to that predicted by an implicit-solvent model that assigns a uniform relative permittivity corresponding to that of the bulk solvent throughout the entire system volume [34, 35]. In light of this result, further quantitative details of this basic comparison between

explicit- and implicit-solvent formulations should be pursued using atomistic models.

#### 1.4 Software for theoretical studies of sequence-dependent LLPS

This chapter is not a comprehensive review of theoretical and computational approaches to biomolecular condensates. This chapter is intended as a practical guide for readers who are interested in applying the above-described theoretical methods, serving as an introduction to the computer codes we have developed to perform the pertinent numerical calculations. Accordingly, the presentation of analytical formulations below is minimal; and we will refer readers to the published literature for much of the mathematical details whenever they are available. The codes written by us for LLPS investigation and cited in the discussion below are available from the following GitHub software sharing webpages:

[https://github.com/laphysique/Protein\\_RPA](https://github.com/laphysique/Protein_RPA)

[https://github.com/laphysique/FH\\_LLPS\\_simple\\_system](https://github.com/laphysique/FH_LLPS_simple_system)

[https://github.com/jwessen/IDP\\_phase\\_separation](https://github.com/jwessen/IDP_phase_separation)

[https://github.com/mmTanmoy/IDP\\_phase\\_separation](https://github.com/mmTanmoy/IDP_phase_separation)

[https://github.com/laphysique/FTS\\_polyampholyte\\_water](https://github.com/laphysique/FTS_polyampholyte_water)

which may also be accessed via the links on our group’s webpage for LLPS software:

[https://arrhenius.med.utoronto.ca/~chan/llps\\_software.html](https://arrhenius.med.utoronto.ca/~chan/llps_software.html)

#### 1.5 Coarse-grained explicit-chain simulation and other approaches

In addition to analytical theories, a very brief summary is also provided below for a coarse-grained, explicit-chain molecular dynamics methodology for studying amino acid sequence-dependent LLPS [36] that relies on a protocol for efficient equilibration by initializing simulation with a highly condensed polymer slab in an elongated rectangular simulation box [37]. Among the method’s many applications (e.g., refs. [21, 38]), its results have been utilized—as mentioned above—to assess RPA [29, 30] and FTS [25] predictions as well as to evaluate [34] common coarse-grained LLPS potentials [36] for their adequacy in describing  $\pi$ -related interactions in LLPS [39] and IDP interactions in general [40, 41].

Besides the methods mentioned above, it should be noted that other theoretical/computational approaches, including lattice [42–44], patchy particle [45, 46], and restricted primitive [47, 48] models, have provided important insights to biomolecular condensates as well; but they are beyond the scope of this chapter.

#### 1.6 Step-by-step practical guides to software

In the presentation below, numerous references will be made to the specific codes available via the webpages listed in Sect. 1.4 above for readers who are interested in test-running them to facilitate understanding of the theoretical formulations and/or to use the codes with appropriate adjustments to perform computations for their own research efforts. For beginners in the field, we have compiled several additional “Practical guides” sections in the discussion below to provide more detailed, step-by-step recipes for obtaining

the data necessary to produce some of the figures in this chapter. These should serve as useful, concrete examples of how the codes work in practice.

## 2 Construction of Phase Diagrams from Analytical Free Energy Functions

Analytical theories for LLPS allow for numerical efficiency when the free energy of a given system,  $f$ , is provided as a function of the concentrations  $\rho$ 's of the constituents:

$$f = f(\rho_1, \rho_2, \dots, \rho_n, \rho_w) . \quad (1)$$

Here, as is customary in the polymer theory literature, the free energy  $f$  is given in units of  $Vk_B T$ , where  $V$  is system volume,  $k_B$  is Boltzmann's constant, and  $T$  is absolute temperature. As such,  $f$  is a Helmholtz free energy defined for a system with constant  $V$  rather than a Gibbs free energy defined for a system under constant pressure  $P$ . Nonetheless, Helmholtz and Gibbs free energies for biomolecular LLPS under ambient conditions are expected to be similar because of relatively small  $PV$  contributions to Gibbs free energy under those conditions. It should be noted, however, that  $PV$  contributions can be substantial for biomolecular LLPS under high hydrostatic pressures as experienced in the deep sea [11]. We do not consider high- $P$  LLPS in this chapter.

In Eq. 1,  $\rho_1, \rho_2, \dots, \rho_n$  are the concentrations for  $n$  solute species, and  $\rho_w$  is solvent concentration. A subscript "w" is used for solvent because water is the most common solvent in biological systems. The  $\rho$ 's may be given as number densities or volume fractions. When the  $\rho$ 's are volume fractions (note that volume fractions are often denoted by  $\phi$ 's in the literature),  $(\sum_{i=1}^n \rho_i) + \rho_w = 1$  by definition.

In such theories, the system with a single phase is macroscopically homogeneous. Local fluctuations in  $\rho$ 's are effectively taken into account by analytical methods, mostly via various perturbative approaches, such that an  $f$  in the form of Eq. 1 may be arrived at without intensive numerical calculation. These analytical theories include, but are not limited to:

- Flory-Huggins theory [12],
- Overbeek-Voorn theory [13],
- Flory-Stockmayer gelation theory [12, 49],
- Polymer cluster theory [50, 51],
- Wertheim's thermodynamic perturbation theory (TPT) [52, 53],
- Random-phase approximation (RPA) theory [16–19, 24], and
- Renormalized-Gaussian fluctuation / random-phase-approximation (RGF/rG-RPA) theory [28, 54].

We now provide a guide to the basic general procedure for extracting information about phase behaviors from  $f(\rho_1, \rho_2, \dots, \rho_n, \rho_w)$  in the form of phase diagrams, irrespective of how  $f(\rho_1, \rho_2, \dots, \rho_n, \rho_w)$  is derived.

## 2.1 Spinodal decomposition

The impact of fluctuations in solvent and solute concentrations on the stability of the system may be examined by the following Taylor series expansion of the free energy  $f$  around any set of concentrations  $\{\rho_i\} \equiv \{\rho_1, \rho_2, \dots, \rho_n, \rho_w\}$  (note that the index  $i$  now covers the solvent as well, i.e.,  $i = 1, 2, \dots, n, w$ ):

$$f(\{\rho_i + \delta\rho_i\}) = f(\{\rho_i\}) + \sum_i \frac{\partial f}{\partial \rho_i} \delta\rho_i + \frac{1}{2} \sum_{i,j} \frac{\partial^2 f}{\partial \rho_i \partial \rho_j} \delta\rho_i \delta\rho_j + O(\delta\rho^3), \quad (2)$$

where the derivatives are evaluated at  $\{\rho_i\}$ . The system is deemed thermodynamically stable if the partition function of the fluctuations, i.e., the integral of  $\exp(-f)$  over the  $\delta\rho_i$ 's, is finite. Considering terms for  $f$  in Eq. 2 through second order in  $\delta\rho_i$ 's while recognizing that the contribution from the  $f$  term linear in  $\delta\rho_i$  to  $\exp(-f)$  may be absorbed into a term quadratic in  $\delta\rho_i$  in the argument for the exponential by the usual procedure of linear shifting of integration variables for Gaussian integrals, this condition for stability amounts to requiring the Hessian matrix  $\hat{\mathcal{H}}$ , with matrix elements

$$\hat{\mathcal{H}}_{ij} = \frac{\partial^2 f}{\partial \rho_i \partial \rho_j}, \quad (3)$$

to be positive definite—meaning that  $\hat{\mathcal{H}}$  is symmetric (which follows automatically from Eq. 3 for any smooth, real-number function  $f$ ) and that all its eigenvalues are positive ( $> 0$ ). Physically, the all-positive-eigenvalues condition ensures that the homogeneous solution phase is stable against any  $\{\delta\rho_i\}$  fluctuations in solute and solvent concentrations. Spinodal decomposition occurs when at least one of the eigenvalues of  $\hat{\mathcal{H}}$  becomes zero, at which point the determinant of the matrix vanishes, i.e.,

$$\det \hat{\mathcal{H}} = 0. \quad (4)$$

Conversely,  $\hat{\mathcal{H}}$  being not positive definite implies global instability of the homogeneous solution phase, manifested experimentally by spinodal decomposition. It should be emphasized, however, that although  $\det \hat{\mathcal{H}} = 0$  defines the spinodal boundary and that  $\det \hat{\mathcal{H}} < 0$  always indicates that there is at least one negative eigenvalue and therefore the homogeneous solution phase is not stable,  $\det \hat{\mathcal{H}} > 0$ , in contrast, does not guarantee that the homogeneous solution phase is thermodynamically stable [24]. The homogeneous solution phase is not stable when  $\hat{\mathcal{H}}$  has one or more negative eigenvalues, because it is unstable against fluctuations along any of the eigenvectors associated with those negative eigenvalues. However,



while an odd number of negative eigenvalues leads to  $\det \hat{\mathcal{H}} < 0$ , an even number of negative eigenvalues results in  $\det \hat{\mathcal{H}} > 0$ . Hence, instability of the homogeneous solution phase can, in some cases, be concomitant with  $\det \hat{\mathcal{H}} > 0$ . In other words,  $\det \hat{\mathcal{H}} < 0$  is sufficient but not necessary for spinodal decomposition.

In the case of incompressible two-component systems that satisfy  $\rho + \rho_w = 1$  (without loss of generality, the unit for concentration is chosen such that the maximum concentration is unity, see example in Fig. 1), there is only one independent concentration variable and thus the Hessian matrix  $\hat{\mathcal{H}}$  reduces to a single second derivative. It follows that the boundary condition for spinodal instability,  $\det \hat{\mathcal{H}} = 0$ , takes the form of

$$f''(\rho) \equiv \frac{\partial^2 f}{\partial \rho^2} = 0. \quad (5)$$

When  $\rho$  is allowed to vary under some—but not all—fixed environmental conditions (temperature, hydrostatic pressure, etc. [11]), there are two  $\rho$ 's satisfying the spinodal boundary condition Eq. 5, one on the dilute (relatively smaller- $\rho$ ) side and the other on the condensed (relatively larger- $\rho$ ) side of the free energy function (Fig. 1a, open circles). When environmental conditions such as temperature that affect the interaction strength (symbolized as  $u$ ) are varied, the free energy function  $f$  also varies accordingly. At a certain interaction strength  $u_{\text{cr}}$  at which the  $\rho$  values for the two spinodal boundaries merge into a single  $\rho = \rho_{\text{cr}}$ , the  $u_{\text{cr}}$  and  $\rho_{\text{cr}}$  are recognized as the critical interaction strength and critical concentration (hence the subscript “cr”), respectively. These two critical quantities are determined by the equations

$$f''(\rho_{\text{cr}}, u_{\text{cr}}) \equiv \left. \frac{\partial^2 f}{\partial \rho^2} \right|_{\rho=\rho_{\text{cr}}, u=u_{\text{cr}}} = 0 \quad (6a)$$

$$f'''(\rho_{\text{cr}}, u_{\text{cr}}) \equiv \left. \frac{\partial^3 f}{\partial \rho^3} \right|_{\rho=\rho_{\text{cr}}, u=u_{\text{cr}}} = 0. \quad (6b)$$

The interaction strength  $u$  is characterized by different parameters in different models. For instance, in FH theory,  $u$  corresponds to the  $\chi$  parameter; in RPA for electrostatics,  $u$  can be quantified by the Bjerrum length  $l_{\text{B}}$ .

The critical interaction strength  $u_{\text{cr}}$  may be obtained through minimizing the function  $u = u(\rho)$  defined implicitly by the spinodal condition  $f''(\rho, u(\rho)) = 0$  because  $u_{\text{cr}}$  is the *weakest* interaction strength that allows for phase separation. Numerically,  $u(\rho)$  can be determined by a root-finding algorithm such as Newton's method or bisection method. Subsequently,  $(\rho_{\text{cr}}, u_{\text{cr}})$  can be solved by minimization algorithms such as the Nelder-Mead method [55] or BFGS method [56]. A pseudocode for this procedure is as follows:

```

def critical_point():
    rho_c, u_c = minimization(u_spinodal, var=rho)
    return rho_c, u_c

def u_spinodal(rho):
    u_sol = root_find(ddf, var=u, const=rho)
    return u_sol

```

Once the critical point is located, it is guaranteed that for all  $u > u_{\text{cr}}$ , there is only one solution for  $f''(\rho) = 0$  in the  $(0, \rho_c)$  range and one solution in the  $(\rho_c, 1)$  range; and bisection root-finding algorithms can be applied to locate the two spinodal concentrations.

Regarding the interaction strength  $u$ , it should be noted that while  $u = u(T) \propto 1/T$  is often assumed in idealized models with a temperature-independent energy scale  $\mathcal{E}$  such that  $u(T) \sim \mathcal{E}/T$  (the Bjerrum length  $l_B$  is an example of this type of  $u$ ), the  $T$ -dependence of interaction strengths of the aqueous solvent-mediated interactions underlying biomolecular condensates is often more complex. In those cases, instead of being a constant,  $\mathcal{E}$  depends on  $T$ , i.e.,  $\mathcal{E} \rightarrow \mathcal{E}(T)$ , and  $u(T)$  is not necessarily a monotonic function of  $T$  (unlike  $u \propto 1/T$ ). For instance, the  $u(T)$  for hydrophobic interaction has a maximum at  $T_{\text{max}} \approx 25^\circ\text{C}$  (see, e.g., the  $\chi(T)$  function in Fig. 2 of ref. [59]). This means that a hydrophobicity-driven LLPS may entail two  $u_{\text{cr}}$  values, one corresponding to a higher critical temperature,  $T_{\text{cr}}^{\text{UCST}}$ , which is an upper critical solution temperature (UCST), and the other a lower critical temperature,  $T_{\text{cr}}^{\text{LCST}}$ , which is a lower critical solution temperature ( $T_{\text{cr}}^{\text{UCST}} > T_{\text{cr}}^{\text{LCST}}$ ) [10, 11, 60]. The physical reason behind this phenomenon is that LLPS is impossible for  $T > T_{\text{cr}}^{\text{UCST}}$  because configuration entropy overwhelms favorable interchain interaction at high temperatures; and LLPS is also impossible for  $T < T_{\text{cr}}^{\text{LCST}}$  because of the weakening of hydrophobic interactions at low temperatures. When performing numerical calculations for model systems embodying this feature, one has to treat the region in which  $u(T)$  increases with increasing  $T$  and the region in which  $u(T)$  decreases with increasing  $T$  separately so that the mapping from  $u$  to  $T$ , i.e., the inverse function  $T = u^{-1}(u(T))$ , can be defined.

## 2.2 Coexisting phases

The spinodal condition signifies divergences in concentration fluctuations and global breakdown of solution homogeneity. In contrast, when the interaction strength of a system is gradually increased in experiments, the phase separation state that is first observed is composed of multiple *coexisting* thermodynamically *stable* phases in which local concentration fluctuations do not diverge. This phenomenon is referred to as binodal phase separation.

The coexisting phases satisfy a balance requirement under which the chemical potentials for each type of solute across all phases are identical, and the osmotic pressure (which depends on the chemical potential of solvent) [18] is also identical across all phases. In

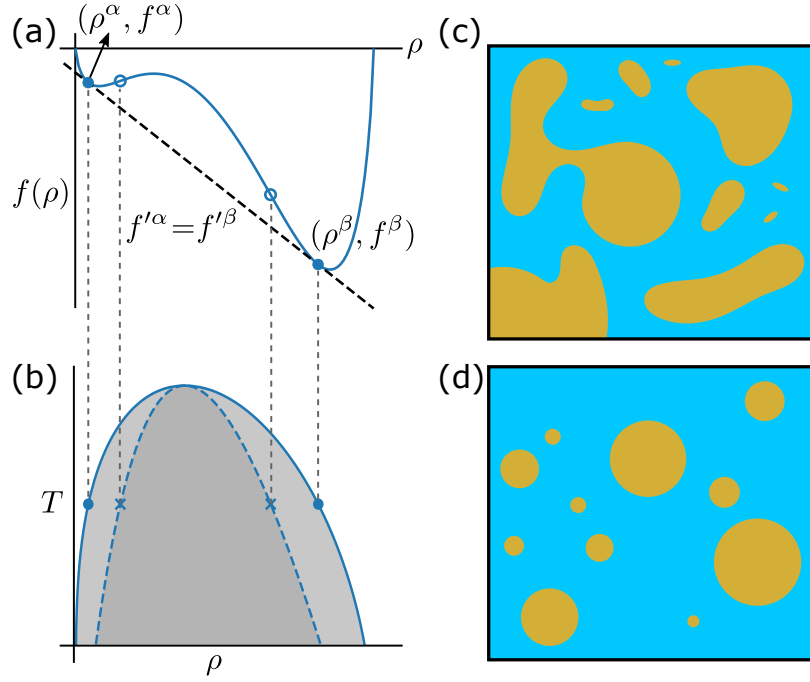


FIG. 1: Construction of the spinodal and binodal (coexistence) phase boundaries. An illustrative example is shown for the procedure described in the text and in ref. [18]. (a) Free energy in units of  $Vk_B T$ ,  $f(\rho)$ , is given by the blue curve for one selected temperature. The  $f''(\rho) = 0$  inflection points for the spinodal phase boundary (Eq. 5) are marked by the two open circles. The common tangent (inclined dashed line) of the two coexistence phases for binodal phase separation is determined by the two equalities in Eq. 10 to obtain the coexisting concentrations  $\rho^\alpha$  and  $\rho^\beta$  marked by the two filled circles. (b) The spinodal (dashed blue curve) and binodal (solid blue curve) phase boundaries are constructed by joining the  $\rho$  values of the open and filled circles in (a), respectively, at different temperatures, as indicated by the vertical dashed lines between (a) and (b). Here  $T$  is absolute temperature. The shaded regions represent the spinodal (darker) and binodal (lighter) regimes of the phase diagram. Results in (a) and (b) are those of a FH model with  $f(\rho) = (\rho/N) \ln \rho + (1 - \rho) \ln(1 - \rho) + \chi \rho(1 - \rho)$ ,  $N = 3$ , and  $T = 1/\chi$  (same as that in Fig. 1 of ref. [10]); the  $f(\rho)$  curve in (a) is for  $\chi = 1.7$ . (c) and (d): Cartoons of spinodal decomposition (c) and droplet formation in binodal phase separation (d), wherein solute is depicted in gold and solvent in cyan. Microscopic images of IDP spinodal decomposition and binodal phase separation can be found, e.g., for Ddx4 in Fig. 7 of ref. [18] and Fig. 3 of ref. [9] respectively.

other words, in a solution of  $n$  solute species that separate into  $m$  coexisting phases,

$$\mu_i^\alpha = \mu_i, \quad \Pi^\alpha = \Pi, \quad (7)$$

where  $\mu$  denotes chemical potential and  $\Pi$  denotes osmotic pressure;  $i, \alpha$  are labels, respectively, for solute species and phases;  $\mu_i$  is the chemical potential common to solute type  $i$  across all phases (same for all  $\alpha$ ). Similarly,  $\Pi$  is the common osmotic pressure across all phases (again, same for all  $\alpha$ ).

By definition, the chemical potential of solute  $i$  in phase  $\alpha$  is given by

$$\mu_i^\alpha = f_i'^\alpha \equiv \left. \frac{\partial f}{\partial \rho_i} \right|_{\rho_i = \rho_i^\alpha}, \quad (8)$$

and the osmotic pressure in phase  $\alpha$  is given by

$$\Pi^\alpha = f^\alpha - \sum_{i=1}^n \rho_i^\alpha f_i'^\alpha, \quad (9)$$

where the free energy  $f^\alpha \equiv f(\rho_1^\alpha, \rho_2^\alpha, \dots, \rho_n^\alpha, \rho_w^\alpha)$ . For binary phase separation in an incompressible two-component ( $n = 1$ ) system with  $\rho_1 + \rho_w = 1$ , there is only one independent concentration variable  $\rho_1$ . Accordingly, the balance requirement for coexisting phases  $\alpha, \beta$  can be simplified by combining the general conditions in Eqs. 8 and 9 and using  $\rho$  to denote solute concentration  $\rho_1$  (as in Eq. 5) to yield

$$f'^\alpha = f'^\beta = \frac{f^\alpha - f^\beta}{\rho^\alpha - \rho^\beta}, \quad (10)$$

which is the *common tangent* condition illustrated in Fig. 1a.

Mapping the coexisting (binodal) condition and the spinodal condition (Sect. 2.1) in Fig. 1a onto a solute concentration-temperature plot yields the phase diagram in Fig. 1b. Cartoons of spatial variation of concentration in spinodal and binodal phase separations are provided in Fig. 1c and d.

Besides the above consideration of chemical potential and osmotic pressure, the balance requirement for coexisting phases can also be derived by minimizing the system free energy,

$$f_{\text{sys}} = \sum_{\alpha=1}^m v^\alpha f^\alpha, \quad (11)$$

under the constraints of volume and mass conservation, viz.,

$$\sum_{\alpha=1}^m v^\alpha = 1, \quad \sum_{\alpha=1}^m v^\alpha \rho_i^\alpha = \rho_i^{\text{bulk}}, \quad (12)$$

where  $v^\alpha$  is the fractional volume in phase  $\alpha$ , and  $\rho_i^{\text{bulk}}$  is the overall concentration of solute  $i$  averaged over the entire system volume. As an example, for an incompressible two-component system,  $f^\alpha = f(\rho^\alpha)$ ,  $f^\beta = f(\rho^\beta)$ , thus, by denoting  $v^\alpha$  as  $v$  and therefore  $v^\beta = 1 - v$ ,

$$f_{\text{sys}} = f_{\text{sys}}^{\text{2comp}} = v f(\rho^\alpha) + (1 - v) f\left(\rho^\beta = \frac{\rho^{\text{bulk}} - v\rho^\alpha}{1 - v}\right). \quad (13)$$

Because  $f_{\text{sys}}^{2\text{comp}}$  is a function of variables  $v$  and  $\rho^\alpha$ , the minimum of  $f_{\text{sys}}^{2\text{comp}}$  is determined by

$$\frac{\partial f_{\text{sys}}^{2\text{comp}}}{\partial \rho^\alpha} = \frac{\partial f_{\text{sys}}^{2\text{comp}}}{\partial v} = 0, \quad (14)$$

yielding

$$v f'^\alpha - v f'^\beta = 0, \quad (15a)$$

$$f^\alpha - f^\beta + f'^\beta (\rho^\beta - \rho^\alpha) = 0, \quad (15b)$$

which are precisely the equations for solving the common tangent in Eq. (10).

### 2.3 Systems with three or more components

For incompressible three-component systems satisfying  $\rho_1 + \rho_2 + \rho_w = 1$ , there are two independent concentration variables. When  $\rho_1$  and  $\rho_2$  are chosen as independent variables, it follows from Eq. 4 that the boundary condition for the spinodal region is given by

$$\det \hat{\mathcal{H}} = \begin{vmatrix} \frac{\partial^2 f}{\partial \rho_1^2} & \frac{\partial^2 f}{\partial \rho_1 \partial \rho_2} \\ \frac{\partial^2 f}{\partial \rho_2 \partial \rho_1} & \frac{\partial^2 f}{\partial \rho_2^2} \end{vmatrix} = 0. \quad (16)$$

To exemplify how this condition is applied, Fig. 2 provides the free energy surface (Fig. 2a) of a simple three-component system, its spinodal region (Fig. 2b and c), and the initial steps for determining the region (Fig. 2b). As shown by the 25 grid points in Fig. 2b, the spinodal region can be determined approximately by a grid search for the area with  $\det \hat{\mathcal{H}} < 0$ . In practice, a denser grid should be used than that shown in Fig. 2b to arrive at a better-approximated spinodal region, which can then be used as a stepping stone to arrive at a much more precise spinodal region by utilizing the numerical techniques described below. Formulations of three-component LLPS have recently been applied to study systems with two polyampholytes with different charge patterns (as model IDPs) [24] and models of natural IDP solutions with salt [28]. In this connection, it is worth noting that short-chain (small  $N$ ) FH models similar to those used in Fig. 1 and Fig. 2 for illustration can be useful for modeling LLPS of folded proteins as well [57, 58]. A step-by-step practical guide to the calculations in these simple FH models are discussed in Sect. 2.5 below.

In studies of three-component systems, phase behaviors are often provided by two-dimensional phase diagrams with solute concentrations  $\rho_1$  and  $\rho_2$  as variables at a given interaction strength. To construct such phase diagrams, one may start with the spinodal region, which can be determined by sampling a grid on the  $\rho_1$ - $\rho_2$  plane to identify the  $(\rho_1, \rho_2)$  values on the grid for which  $\det \hat{\mathcal{H}} < 0$ , as illustrated above in Fig. 2b. Another example is now provided in Fig. 3a. With a sufficiently dense grid, this is an efficient way to identify the approximate spinodal region. As will be explained below, this approximate

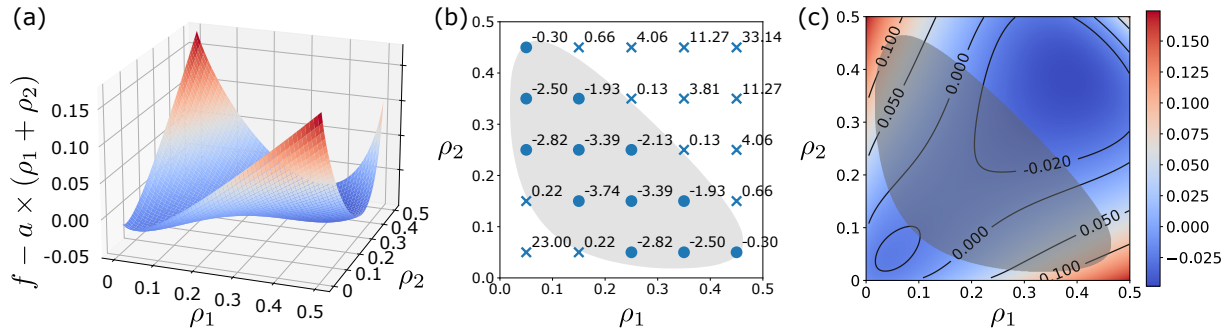


FIG. 2: Three-component phase separation. Shown here is an example free energy surface of a solution containing two solute species with overall concentrations  $\rho_1$  and  $\rho_2$  in a solvent, as a three-dimensional plot (a) with its spinodal region (b) and as an equivalent contour plot (c). Free energy  $f$  in (a) and (c) is color coded by the scale in (c). The region shaded in grey in (b) and (c) is the spinodal area defined by the boundary condition in Eq. 16. This example is a FH model with  $f(\rho_1, \rho_2) = (\rho_1/N) \ln \rho_1 + (\rho_2/N) \ln \rho_2 + (1 - \rho_1 - \rho_2) \ln(1 - \rho_1 - \rho_2) - \chi[\rho_1\rho_2 + 0.3\rho_1(1 - \rho_1) + 0.3\rho_2(1 - \rho_2)]$  and  $N = 3$ , where  $\chi = 1.7$  is used. As in Fig. 2a of ref. [24], a term linear in  $\rho_1$  and  $\rho_2$  is included in the variable for  $f$  to highlight variation in curvature of the  $f(\rho_1, \rho_2)$  function. Such a shift in free energy has no effect on phase separation. The same free energy variable with  $a = -0.72505$  is used throughout this figure. To illustrate how the spinodal region is determined computationally, the  $\det \hat{\mathcal{H}}$  (Eq. 16) values at 25 example grid points on the  $\rho_1$ — $\rho_2$  plane are provided in (b). The grid points are depicted as circles when  $\det \hat{\mathcal{H}} < 0$  and as crosses when  $\det \hat{\mathcal{H}} > 0$ . We have also conducted an extensive numerical check to verify that the Hessian matrix  $\hat{\mathcal{H}}$  has two positive eigenvalues in the  $\det \hat{\mathcal{H}} > 0$  region of this example.

spinodal region is important as a starting point to efficiently map out the coexisting region as well. To arrive at an accurate spinodal boundary beyond the rough boundary afforded by the grid search, we seek to determine the spinodal boundary as a mapping between  $\rho_1$  and  $\rho_2$  by numerically solving the pertinent mathematical relations. To facilitate this determination, we first separate the spinodal region into an upper part (with larger  $\rho_2$  values) and a lower part (with smaller  $\rho_2$  values) with a demarcation at or near the  $\rho_2$  value for which the spinodal region's extent in the  $\rho_1$  direction is the widest (Fig. 3b, horizontal dashed line) so that most likely  $\rho_1$  is mapped onto only one value of  $\rho_2$  in each of the two parts of the spinodal region. This step is necessary since it allows us to construct the spinodal boundary as two separate mathematical functions  $\rho_2(\rho_1)$ , one for the upper part and one for the lower part of the spinodal region. Otherwise, in the absence of this separation of the spinodal region, one  $\rho_1$  value is always mapped onto two  $\rho_2$  values (and vice versa) when the entire spinodal boundary is considered as a whole, in which case a mathematical function in the form of  $\rho_2(\rho_1)$  is not defined ( $\rho_1$  maps onto multiple values of  $\rho_2$ ). Now,  $\rho_2(\rho_1)$  can be solved separately for the two parts by applying the pseudocode `u_spinodal(rho)` mentioned in Sect. 2.1 above by treating  $\rho_2$  as  $u$  and substituting  $\rho_1$  for the variable `rho`. As an illustration, this procedure is used to obtain the grey-shaded spinodal area for the example free energy surface in Fig. 2b.

For coexisting phases (binodal phase separation), the same correspondence between balancing of chemical potentials and free energy minimization for binary phase separation of an incompressible three-component system is described in ref. [24] (see, in particular, Eqs. 11–22 of this reference). For systems with more components and more separated phases, the form of  $f_{\text{sys}}$  as defined by Eqs. 11 and 12 can be too complicated for algebraic minimization algorithms. In those cases, more numerically intense algorithms such as Monte Carlo methods may be applied [61].

In numerical calculations, the common tangent equation in Eq. (10) can be solved via multidimensional root-finding algorithms, such as Broyden’s method [62] or modified Powell’s method [63]; the minimization of  $f_{\text{sys}}$  can be solved by multidimensional minimization algorithms such as L-BFGS-B [64] and SLSQP [65] methods. It should be noted that multidimensional root-finding and minimization algorithms are often sensitive to the initial guess of the solutions. In many cases, a random search for a proper initial guess is required to arrive at the correct roots or global minimum. Therefore, it would be helpful if the numerical search can be constrained to a smaller regime. With this in mind, it is noteworthy that when interaction strength or solute concentration of a homogeneous solution is varied, binodal phase separation—with a mechanism akin to nucleation—ensues *before* spinodal instability, suggesting that the spinodal boundary is always enclosed by the coexisting boundary (the spinodal region is a subset of the region enclosed by the coexisting boundary). Since determining the spinodal region is numerically efficient, the above consideration implies that one can first determine the spinodal region and then use the concentrations within the region—which is then known to be unstable against phase separation—as input to numerical algorithms for solving the coexisting (binodal) phase boundary. We find that this is indeed a cost-effective protocol. An example of such a calculation is described in Fig. 3c and d.

## 2.4 Available software

Some of the software we developed to perform numerical calculations for the RPA and rG-RPA theories mentioned above are available from the webpage [https://github.com/laphysique/Protein\\_RPA](https://github.com/laphysique/Protein_RPA) of the Github repository.

For systems with one polymer species and salt at a given concentration (i.e., salt concentration is an input parameter, which can be zero or any other chosen value, and treated as a constant during the execution of the code), the energy minimization solvers for common tangent construction are in `f_min_solve_1p_1salt.py`, `f_min_solve_1p_1salt_LCST.py`, and `fmin_rgRPA_1p_1salt.py` for different systems. These scripts are used for plotting phase diagrams with temperature/interaction strength as variable. A “one button for all” script for each of these systems is also available as `ps_main_1p_1salt.py`, `ps_main_1p_1salt_LCST.py`, and `rgRPA_main.py` to directly output the spinodal and binodal phase separation concentrations in a temperature range for a given sequence and a salt concentration. However, users will need to tune the parameters of these “one button for all” scripts to ensure that they work

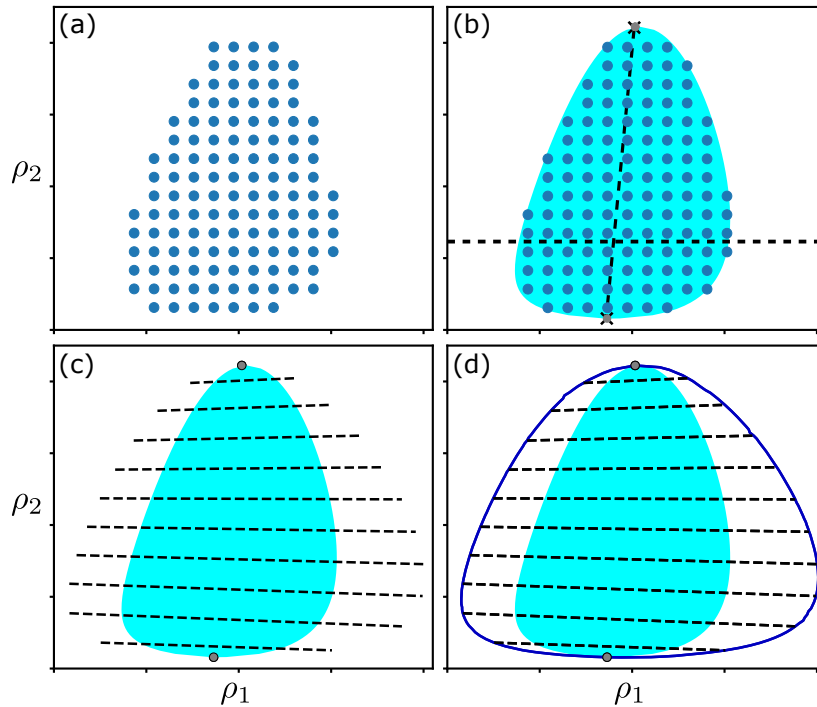


FIG. 3: Construction of phase diagram of a three-component system with tie lines linking pairs of coexisting solute concentrations. (a) Conduct a grid search to determine an approximate  $\det \hat{\mathcal{H}} < 0$  spinodal region [marked by cyan shading in (b)–(d)]. (b) Choose a  $\rho_2$  value separating the spinodal region into an upper and a lower parts at or near where the  $\rho_1$ -extent of the region is widest (horizontal dashed line); then locate the maximum  $\rho_2$  in the upper part and the minimum  $\rho_2$  in the lower part (crosses) on the  $\det \mathcal{H} = 0$  boundary of the approximate spinodal region. (c) Use points along the line linking the maximum and minimum of  $\rho_2$  [near-vertical inclined dashed line in (b)] as initial bulk concentrations  $(\rho_1^{\text{bulk}}, \rho_2^{\text{bulk}})$ ; calculate the final binodal phase-separated concentrations  $\alpha = (\rho_1^\alpha, \rho_2^\alpha)$  and  $\beta = (\rho_1^\beta, \rho_2^\beta)$  by minimizing system free energy using the prescription for three-component phase separation described by Eqs. 11–22 of ref. [24] (note that the three conditions in Eq. 22 of ref. [24] is the three-component equivalent of the two conditions in the two-component Eq. 15 in this chapter). Then connect  $\alpha, \beta$  by dashed lines as tie lines. The points marked by crosses in (b) are now marked by circles in (c) and (d) as critical points. (d) Connect all  $\alpha$  and  $\beta$  points together with the upper and lower critical points to obtain the binodal phase boundary. Data for this example are those of the theoretical rG-RPA phase diagram of Ddx4 at pH = 7.0 in Fig. 5a of ref. [28]. An extensive numerical check has been conducted to verify that the  $\hat{\mathcal{H}}$  is positive definite in the  $\det \hat{\mathcal{H}} > 0$  region of this example.

well for their polymer system of interest.

For systems with one polymer species and variable salt concentration, the script `fsalt_rGRPA_1p_1salt.py` is for solving polymer-salt two-dimensional phase diagrams in rG-RPA theory (tracking changes in polymer as well as salt concentrations). This script has been applied in ref. [28]. The corresponding “one button for all” script is `rgRPA_main.salt.py`. In situations when the performance of this code is not robust, the



script `rgRPA_salt_main_auto.py` may be used to perform part of the task. For instance, `rgRPA_salt_main_auto.py`, which is relatively more robust, is employed to perform the calculation described in Fig. 3c and d, while scripts specialized to the system of interest are needed to be written anew to conduct the grid search and partition of the putative spinodal region as described in Fig. 3a and b.

Functions for the free energy minimization solver for two-polymer RPA system are in `f_min_solve_2p_0salt.py`. This code, which is used in ref. [24], is for obtaining two-dimensional phase diagrams with the concentrations of the two polymers as variables. A “one button for all” script for outputting the entire two-dimensional phase boundary is in `ps_main_2p_0salt.py`. It should be noted, however, that the performance of these codes for two-polymer systems are sensitive to the precise form of the free energy function; the parameters in the codes will need to be tuned case by case.

## 2.5 Practical guide to the calculations for Figs. 1 and 2

The specific codes for the FH models used in Figs. 1 and 2 are available in the Jupyter Notebook format via the following Github webpage: [https://github.com/laphysique/FH\\_LLPS\\_simple\\_system/blob/main/FH\\_phase\\_diagram.ipynb](https://github.com/laphysique/FH_LLPS_simple_system/blob/main/FH_phase_diagram.ipynb). Note that this webpage provides only a static image because Github does not support dynamic Jupyter Notebook. Users will need to download the file to their computer with the Jupyter Notebook package installed to run the code, or they may run Jupyter Notebook on Google Drive as follows: (i) Upload the Notebook file `FH_phase_diagram.ipynb` (obtained from the above Github website) to Google Drive. (ii) Double click it. A message “No preview available” will appear. Click the “Open with” button at the center top of the screen, then click “Connect more apps”. (iii) A window of “Google Workplace Marketplace” will show up. Scroll down and click “Colaboratory” and install it (Google will ask you to approve a few items). (iv) After Colaboratory is installed, refresh the Google Drive page and double click the Notebook. The Notebook will then run in a new browser window.

## 3 Field-Theoretic Simulation (FTS)

FTS methods [31], which are capable of modeling sequence-dependent LLPS without invoking some of the approximations in analytical theories such as RPA, are currently foraging in the fast expanding research territories of LLPS in biology [25, 32, 33, 35, 66]. As far as computational cost is concerned, FTS—in this respect it is similar to self-consistent field theory [67]—may be viewed as intermediate between analytical theories such as RPA and explicit-chain simulations. Compared to RPA and rG-RPA, significantly more intense computation is required in FTS to calculate the chemical potentials  $\mu$ 's and osmotic pressure  $\Pi$ 's defined in Eqs. 8 and 9. Nonetheless, because the analytical formulation of FTS reduces the tremendous number of coordinate degrees of freedom of the individual

polymer chains and solvent molecules to relatively few density degrees of freedom, FTS incurs a significantly less computational cost vis-à-vis explicit-chain simulations—especially those with explicit solvent molecules—which keep track of all coordinate degrees of freedom.

### 3.1 Field theory descriptions of polymer solutions

Given the immense complexities of the biological systems, the current focus of FTS model building is to capture the basic physics that drive LLPS in living cells starting from *minimal* interaction Hamiltonians while making least amount of compromise on the accuracy in solving the models. Minimality ensures least number of free parameters, thus offering firm conceptual grasp on the physical factors involved.

To illustrate the usage of FTS, we consider a simple system of volume  $V$  containing  $n_p$  polyampholytes, each consisting of  $N$  beads connected via Gaussian springs (extensively studied using FTS in ref. [32]). On every chain, bead  $\alpha$  is assigned an electric charge  $\sigma_\alpha$  in units of the proton charge, and all beads are modelled as Gaussian distributions  $\Gamma(\mathbf{r}) = \exp(-\mathbf{r}^2/2\bar{a}^2)/(2\pi\bar{a}^2)^{3/2}$  with a common width  $\bar{a}$ . This Gaussian smearing procedure was introduced in ref. [68] to regulate ultraviolet (UV), i.e., short-distance, divergences associated with point interactions. For simplicity, we restrict the discussion in this Section to overall electrically neutral chains, i.e.  $\sum_{\alpha=1}^N \sigma_\alpha = 0$ .

The chains interact via Coulomb forces and short-range excluded volume repulsion. To write down the partition function for this system, we first express the bead and charge densities in the system as, respectively,

$$\hat{\rho}(\mathbf{r}) = \sum_{i=1}^{n_p} \sum_{\alpha=1}^N \Gamma(\mathbf{r} - \mathbf{R}_{i,\alpha}), \quad (17a)$$

$$\hat{c}(\mathbf{r}) = \sum_{i=1}^{n_p} \sum_{\alpha=1}^N \Gamma(\mathbf{r} - \mathbf{R}_{i,\alpha}) \sigma_\alpha, \quad (17b)$$

where  $\mathbf{R}_{i,\alpha}$  is the position vector of bead  $\alpha$  on chain  $i$ . The canonical partition function is then

$$Z = \frac{1}{n_p!} \left( \prod_{i=1}^{n_p} \prod_{\alpha=1}^N \int d\mathbf{R}_{i,\alpha} \right) e^{-\hat{H}_0 - \hat{H}_1 - \hat{H}_2}, \quad (18)$$

where the three terms of the Hamiltonian, in units of  $k_B T$ ,

$$\hat{H}_0 = \frac{3}{2b^2} \sum_{i=1}^{n_p} \sum_{\alpha=1}^{N-1} (\mathbf{R}_{i,\alpha+1} - \mathbf{R}_{i,\alpha})^2, \quad (19a)$$

$$\hat{H}_1 = \frac{v}{2} \int d\mathbf{r} \hat{\rho}(\mathbf{r})^2, \quad (19b)$$

$$\hat{H}_2 = \frac{l_B}{2} \int d\mathbf{r} \int d\mathbf{r}' \frac{\hat{c}(\mathbf{r}) \hat{c}(\mathbf{r}')}{|\mathbf{r} - \mathbf{r}'|}, \quad (19c)$$

provide, respectively, chain connectivity with  $b$  being the reference bond length, excluded volume interactions with  $v$  as the excluded volume parameter, and electrostatic interactions with Bjerrum length  $l_B = e^2/4\pi\epsilon k_B T$ .

A partition function such as Eq. 18 can be turned into the partition function,  $Z$ , of a statistical field theory through the use of Hubbard-Stratonovich transformations [69]. We refer to existing literature for the detailed derivation [31, 70] and simply state the result here:

$$Z = \frac{V^{n_p}}{n_p! Z_w Z_\psi} \int \mathcal{D}w \int \mathcal{D}\psi e^{-H[w, \psi]}, \quad (20)$$

where the field Hamiltonian is

$$H[w, \psi] = -n_p \ln Q[\check{w}, \check{\psi}] + \int d\mathbf{r} \left( \frac{w^2}{2v} + \frac{(\nabla\psi)^2}{8\pi l_B} \right), \quad (21)$$

with

$$Q[\check{w}, \check{\psi}] \equiv \frac{1}{V} \left( \frac{3}{2\pi b^2} \right)^{\frac{3(N-1)}{2}} \left( \prod_{\alpha=1}^N \int d\mathbf{R}_\alpha \right) \exp \left[ -\frac{3}{2b^2} \sum_{\alpha=1}^{N-1} (\mathbf{R}_{\alpha+1} - \mathbf{R}_\alpha)^2 - i \sum_{\alpha=1}^N \left( \check{w}(\mathbf{R}_\alpha) + \sigma_\alpha \check{\psi}(\mathbf{R}_\alpha) \right) \right], \quad (22)$$

wherein  $i^2 = -1$ , being the partition function of a single polymer subject to external chemical potential and electrostatic potential fields  $i\check{w}(\mathbf{r}) = \Gamma \star iw(\mathbf{r}) \equiv \int d\mathbf{r}' \Gamma(\mathbf{r} - \mathbf{r}') iw(\mathbf{r}')$  and  $i\check{\psi}(\mathbf{r}) = \Gamma \star i\psi(\mathbf{r}) \equiv \int d\mathbf{r}' \Gamma(\mathbf{r} - \mathbf{r}') i\psi(\mathbf{r}')$ , respectively. The renormalization factors  $Z_w$  and  $Z_\psi$ , given by

$$Z_w = \int \mathcal{D}w e^{-\int d\mathbf{r} w^2/2v}, \quad (23a)$$

$$Z_\psi = \int \mathcal{D}\psi e^{-\int d\mathbf{r} (\nabla\psi)^2/8\pi l_B}, \quad (23b)$$

are physically inconsequential, but are included for numerical convenience since they cancel UV divergences associated with arbitrarily small fluctuations in  $w$  and  $\psi$ . This can be understood as follows: The Gaussian smearing removes Fourier modes from  $w$  and  $\psi$  with wave numbers  $k \equiv |\mathbf{k}| \gtrsim \bar{a}^{-1}$ , such that these modes are not present in  $Q[\check{w}, \check{\psi}]$  in the field Hamiltonian in Eq. 21. The UV parts of  $\int \mathcal{D}w \int \mathcal{D}\psi e^{-H[w, \psi]}$  and  $Z_w Z_\psi$  therefore exactly match, and therefore cancel in the field theory partition function in Eq. 20.

### 3.2 Complex-Langevin sampling

The complex nature of  $H[w, \psi]$  is problematic for many standard Monte Carlo methods since  $\exp(-H[w, \psi])$  cannot be interpreted as a probability weight for a field configuration. This problem, known as the “sign problem”, can be tackled using Complex-Langevin (CL) sampling [71, 72], which is closely related to the formulation for stochastic quantization in theories of quantum fields [73–75]. CL sampling has been shown to constitute

an efficient approach to polymer field theories [70]. The CL method introduces a fictitious time-dependence on the fields, after analytically continuing them to their complex planes [ $w(\mathbf{r}) \rightarrow w(\mathbf{r}, t)$  and  $\psi(\mathbf{r}) \rightarrow \psi(\mathbf{r}, t)$ ], that is governed by the stochastic differential equations

$$\frac{\partial \phi(\mathbf{r}, t)}{\partial t} = -\frac{\delta H[w, \psi]}{\delta \phi(\mathbf{r}, t)} + \eta_\phi(\mathbf{r}, t), \quad \phi = w, \psi \quad (24)$$

for Langevin dynamics evolving in the fictitious time  $t$ , where  $\eta_\phi(\mathbf{r}, t)$  represents real-valued Gaussian noise with zero mean and  $\langle \eta_\phi(\mathbf{r}, t) \eta_{\phi'}(\mathbf{r}', t') \rangle = 2\delta_{\phi, \phi'} \delta(\mathbf{r} - \mathbf{r}') \delta(t - t')$ . Averages in the field picture are then computed as asymptotic CL time averages,

$$\langle \mathcal{O}[w(\mathbf{r}), \psi(\mathbf{r})] \rangle_{\text{F}} = \lim_{t_{\text{max}} \rightarrow \infty} \frac{1}{t_{\text{max}}} \int_0^{t_{\text{max}}} dt \mathcal{O}[w(\mathbf{r}, t), \psi(\mathbf{r}, t)]. \quad (25)$$

For our model in Eq. 19, the functional derivatives of the field Hamiltonian are

$$\frac{\delta H[w, \psi]}{\delta w(\mathbf{r})} = i\tilde{\rho}(\mathbf{r}) + \frac{1}{v}w(\mathbf{r}), \quad (26a)$$

$$\frac{\delta H[w, \psi]}{\delta \psi(\mathbf{r})} = i\tilde{c}(\mathbf{r}) - \frac{1}{4\pi l_B} \nabla^2 \psi(\mathbf{r}), \quad (26b)$$

where

$$\tilde{\rho}(\mathbf{r}) = in_{\text{p}} \frac{\delta \ln Q[\check{w}, \check{\psi}]}{\delta w(\mathbf{r})}, \quad (27a)$$

$$\tilde{c}(\mathbf{r}) = in_{\text{p}} \frac{\delta \ln Q[\check{w}, \check{\psi}]}{\delta \psi(\mathbf{r})} \quad (27b)$$

are field operators corresponding to bead and charge densities, named so because  $\langle \hat{\rho}(\mathbf{r}) \rangle = \langle \tilde{\rho}(\mathbf{r}) \rangle_{\text{F}}$  and  $\langle \hat{c}(\mathbf{r}) \rangle = \langle \tilde{c}(\mathbf{r}) \rangle_{\text{F}}$ , where, as defined above in Eq. 25,  $\langle \dots \rangle_{\text{F}}$  stands for field average [31]. For a given field configuration  $\{w(\mathbf{r}), \psi(\mathbf{r})\}$ , so-called forwards and backwards chain propagators  $q_F(\mathbf{r}, \alpha)$  and  $q_B(\mathbf{r}, \alpha)$  can be used to calculate the field operators  $\tilde{\rho}(\mathbf{r})$ ,  $\tilde{c}(\mathbf{r})$  and  $Q[\check{w}, \check{\psi}]$ . The chain propagators are constructed iteratively as

$$q_F(\mathbf{r}, \alpha + 1) = e^{-iW(\mathbf{r}, \alpha + 1)} \Phi \star q_F(\mathbf{r}, \alpha), \quad (28a)$$

$$q_B(\mathbf{r}, \alpha - 1) = e^{-iW(\mathbf{r}, \alpha - 1)} \Phi \star q_B(\mathbf{r}, \alpha), \quad (28b)$$

where  $W(\mathbf{r}, \alpha) \equiv \check{w}(\mathbf{r}) + \sigma_\alpha \check{\psi}(\alpha)$ ,  $\Phi(\mathbf{r}) \equiv (3/2\pi b^2)^{3/2} \exp(-3\mathbf{r}^2/2b^2)$ , and starting from

$q_F(\mathbf{r}, 1) = \exp[-iW(\mathbf{r}, 1)]$  and  $q_B(\mathbf{r}, N) = \exp[-iW(\mathbf{r}, N)]$ . One can then show that

$$Q[\check{w}, \check{\psi}] = \frac{1}{V} \int d\mathbf{r} q_F(\mathbf{r}, N), \quad (29a)$$

$$\tilde{\rho}(\mathbf{r}) = \Gamma \star \frac{n_p}{V Q[\check{w}, \check{\psi}]} \sum_{\alpha=1}^N e^{iW(\mathbf{r}, \alpha)} q_F(\mathbf{r}, \alpha) q_B(\mathbf{r}, \alpha), \quad (29b)$$

$$\tilde{c}(\mathbf{r}) = \Gamma \star \frac{n_p}{V Q[\check{w}, \check{\psi}]} \sum_{\alpha=1}^N e^{iW(\mathbf{r}, \alpha)} q_F(\mathbf{r}, \alpha) q_B(\mathbf{r}, \alpha) \sigma_\alpha. \quad (29c)$$

In FTS, the continuous fields are approximated by discrete field variables defined on the sites of a cubic lattice with periodic boundary conditions. As noted above, field fluctuations on scales  $\lesssim \bar{a}$  can be “renormalized away” which means that the lattice spacing  $\Delta x$  should be chosen such that  $\Delta x \lesssim \bar{a}$ . The CL time evolution equations in Eq. 24 are integrated numerically using a finite time-step  $\Delta t$ , where  $\Delta t \eta_w(\mathbf{r}, t)$  and  $\Delta t \eta_\psi(\mathbf{r}, t)$  are random numbers drawn independently for each lattice site and time-step from a normal distribution with zero mean and variance  $\sigma^2 = 2\Delta t / \Delta x^3$ .

A simple Euler stepping method to solve Eq. 24 is possible, but often requires an extremely small time-step  $\Delta t$  to yield numerical stability. The numerical issue is reminiscent of a similar issue in dealing with stiff differential equations, which often can be handled by implicit integration schemes. Several sophisticated numerical methods have been proposed for integrating the CL evolution equations in Eq. 24 that yield improved numerical stability [76]. We here review the first order semi-implicit method of ref. [76], generalized to multiple fields  $\{\phi_i\}$ . Since a fully implicit integration, where  $\delta H / \delta \phi_i$  would be evaluated at  $t + \Delta t$ , is not possible due to the complicated dependence of  $H$  on the fields, the semi-implicit method instead works by replacing the linear part of  $\delta H / \delta \phi_i$  by its value at  $t + \Delta t$ , i.e.,

$$\phi_i(t + \Delta t) = \phi_i(t) + \Delta t \left[ - \left( \frac{\delta H}{\delta \phi_i} \right)_t + \left( \left[ \frac{\delta H}{\delta \phi_i} \right]_{\text{lin}} \right)_t - \left( \left[ \frac{\delta H}{\delta \phi_i} \right]_{\text{lin}} \right)_{t+\Delta t} \right] + \Delta t \eta_i, \quad (30)$$

where  $[\dots]_{\text{lin}}$  denotes taking the linear part in fields. We have here suppressed the spatial dependence for notational convenience. Provided that the quadratic expansion of the field Hamiltonian is expressed in the form

$$H = \int d\mathbf{r} \left( \sum_i a_i \phi_i + \frac{1}{2} \sum_{i,j} \phi_i K_{ij} \phi_j + \mathcal{O}(\phi^3) \right) \quad (31)$$

with  $K_{ij}$  to be determined below, the linear part of  $\delta H / \delta \phi_i$  is

$$\left( \left[ \frac{\delta H}{\delta \phi_i} \right]_{\text{lin}} \right)_t = a_i + \sum_j K_{ij} \phi_j(t). \quad (32)$$

Solving Eq. 30 for  $\phi_i(t + \Delta t)$  gives

$$\phi_i(t + \Delta t) = \phi_i(t) + \mathcal{F}^{-1} \sum_j \left[ (\mathbf{M}^{-1})_{ij} \mathcal{F} \left[ -\Delta t \left( \frac{\delta H}{\delta \phi_j} \right)_t + \Delta t \eta_j \right] \right], \quad (33)$$

where  $\mathcal{F}$  and  $\mathcal{F}^{-1}$  denote Fourier and inverse Fourier transforms, respectively, and  $\mathbf{M}^{-1}$  is the matrix inverse of the matrix  $\mathbf{M}$  whose components are given by

$$(\mathbf{M})_{ij} = \delta_{ij} + \Delta t \hat{K}_{ij}, \quad (34)$$

with  $\hat{K}_{ij}$  being the Fourier representation of  $K_{ij}$ , the corresponding matrix is denoted as  $\hat{\mathbf{K}}$  below. This semi-implicit method yields a much higher level of numerical stability than an Euler integration. However, both integration methods are formally accurate to  $\mathcal{O}(\Delta t)$ , meaning that larger  $\Delta t$  values should still be used with caution. For our particular model of consideration, we can introduce the field basis  $\phi_i = (w, \psi)_i$ . A quadratic expansion of the field Hamiltonian in Eq. 21 can then be shown to give

$$\hat{\mathbf{K}}(k \neq 0) = \begin{pmatrix} \rho \hat{\Gamma}_k^2 g_k^{\text{mm}} + 1/v & \rho \hat{\Gamma}_k^2 g_k^{\text{mc}} \\ \rho \hat{\Gamma}_k^2 g_k^{\text{mc}} & \rho \hat{\Gamma}_k^2 g_k^{\text{cc}} + k^2/4\pi l_B \end{pmatrix}, \quad (35a)$$

$$\hat{\mathbf{K}}(k = 0) = \begin{pmatrix} 1/v & 0 \\ 0 & 0 \end{pmatrix}, \quad (35b)$$

where  $k$  is wave number as before,  $\rho \equiv n_p N/V$  is the bulk density of polymer beads,  $\hat{\Gamma}_k = \exp(-\bar{a}^2 k^2/2)$  is the Fourier transform of  $\Gamma(\mathbf{r})$ , and

$$g_k^{\text{mm}} = \frac{1}{N} \sum_{\alpha, \gamma=1}^N e^{-|\alpha - \gamma| b^2 k^2/6}, \quad (36a)$$

$$g_k^{\text{mc}} = \frac{1}{N} \sum_{\alpha, \gamma=1}^N \sigma_\alpha e^{-|\alpha - \gamma| b^2 k^2/6}, \quad (36b)$$

$$g_k^{\text{cc}} = \frac{1}{N} \sum_{\alpha, \gamma=1}^N \sigma_\alpha \sigma_\gamma e^{-|\alpha - \gamma| b^2 k^2/6} \quad (36c)$$

follow from the expansion of the term  $-n_p \ln Q$  in Eq. 21. The linear part of the field Hamiltonian expansion for our model in Eq. 31 is  $a_i = (-iNn_p, 0)_i$ .

### 3.3 Computational implementation of FTS

We are now in a position to summarize how FTS is done in a computer. First, we discretize the periodic cubic box of volume  $V$  into  $M^3$  voxels, each with volume  $\Delta V = V/M^3$  (Fig. 4a). The continuous fields are now approximated by specifying their values on each

voxels. Next, we follow the steps listed below to self-consistently evaluate the equilibrium evolution of the system dictated by the interaction Hamiltonian Eq. 21.

1. Initialize the fields on each voxel by complex random numbers at the first CL step.
2. Compute the system-specific  $\hat{K}$  matrix necessary for the semi-implicit method (Eqs. 35 and 36).
3. Calculate forward and backward propagators, single-chain partition function, charge and bead density operators using Eqs. 28 and 29.
4. Update the field values on each voxels using Eq. 33.
5. Start the next CL step by repeating steps from step 3 with the new fields.

Equilibration of the system may be monitored, e.g., by plotting  $Q$  vs CL time. Once the system has stabilized, averages of operators can be calculated using Eq. 25. However, field configurations used in averaging should be separated by a sufficient number of CL steps in between to make sure the configurations are uncorrelated. The equilibration of a model system is illustrated in Figs. 4b and c, which show snapshots of the real, non-negative part of the bead density field operator  $\tilde{\rho}(\mathbf{r})$  under single-phase and phase-separating conditions, respectively. These snapshots were generated using the FTS python script available at [https://github.com/jwessen/IDP\\_phase\\_separation/blob/main/FTS\\_polyampholytes.py](https://github.com/jwessen/IDP_phase_separation/blob/main/FTS_polyampholytes.py).

### 3.4 Chemical potential and osmotic pressure

To investigate the propensity for the system to phase separate, we first describe how to compute using FTS and in units of  $k_B T$  the chemical potential  $\mu$  and osmotic pressure  $\Pi$ , defined as

$$\beta\mu = - \left( \frac{\partial \ln Z}{\partial n_p} \right)_V, \quad (37a)$$

$$\beta\Pi = \left( \frac{\partial \ln Z}{\partial V} \right)_{n_p}, \quad (37b)$$

where  $\beta = 1/k_B T$ . (This  $\beta$  should not be confused with the phase label used in Sect. 2). Given how  $\beta\mu$  and  $\beta\Pi$  vary with polymer bead density, the possibility of phase separation can then be studied as follows: Two phases with bead bulk densities  $\rho^{(1,2)} \equiv n_p^{(1,2)} N/V^{(1,2)}$  can coexist in equilibrium if their respective chemical potentials and osmotic pressures match, i.e.  $\beta\Pi(\rho^{(1)}) = \beta\Pi(\rho^{(2)})$  and  $\beta\mu(\rho^{(1)}) = \beta\mu(\rho^{(2)})$ , since the balance of osmotic pressure ensures that the boundary between the two phases is stationary, while the chemical potential balance means that there is no net flow of particles across the phase boundary. The ability for a system to phase separate at a given temperature is therefore manifested by the existence of self-intersection points of the curve  $(\beta\Pi(\rho), \beta\mu(\rho))$  generated by varying  $\rho$  at that temperature [77].

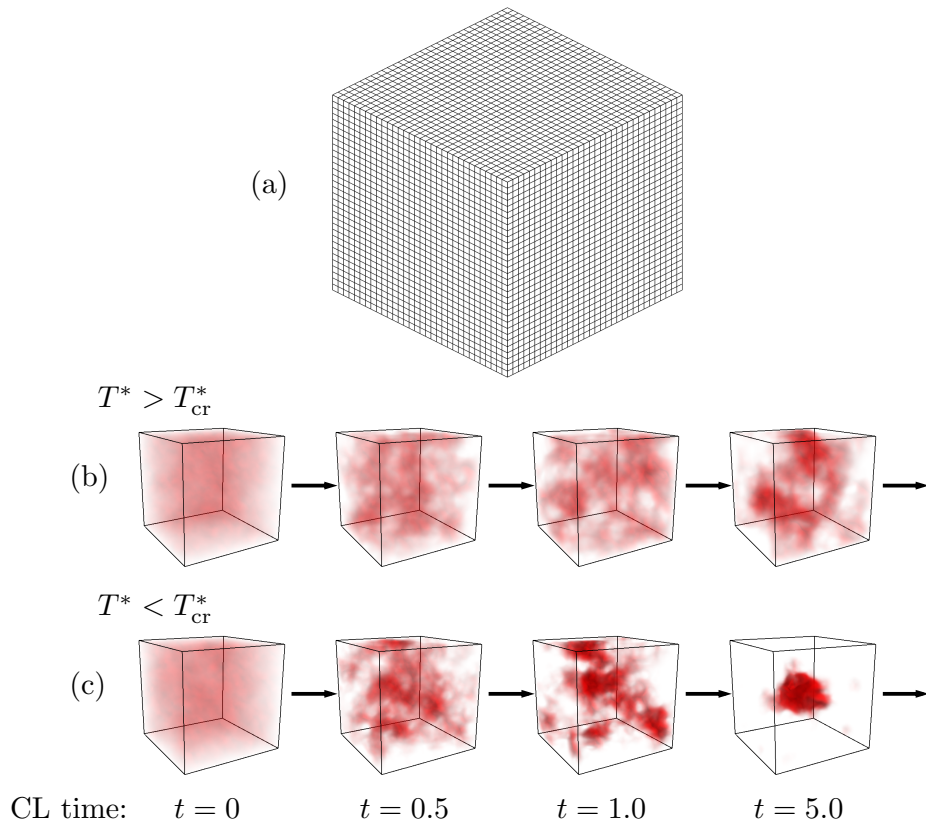


FIG. 4: FTS by CL sampling. (a) Simulation grid. (b) The initial equilibration of a system during FTS, illustrated by snapshots of the real, non-negative part of the polymer bead density operator  $\tilde{\rho}(\mathbf{r})$ . The snapshots were generated by integrating the CL evolution equations on an  $M = 48$  lattice with lattice spacing  $\Delta x = \bar{a}$  and time-step  $\Delta t = 0.01$ , starting from random initial field configurations. The system has a bulk density  $n_p N/V = 0.1b^{-3}$  of sv20 chain beads (charge sequence given in Fig. 6a), described by a smearing length  $\bar{a} = b/\sqrt{6}$  and excluded volume parameter  $v = 0.0068b^3$ . The simulation was performed at a reduced temperature  $T^* \equiv b/l_B = 10.0$  which is sufficiently high to prevent phase separation;  $T_{cr}^*$  is critical temperature. (c) Same as (b), but for  $T^* = 0.1$ . At this lower temperature, the system enters into an inhomogeneous state containing a dense, phase separated droplet in a dilute environment.

The partition functions  $Z$  in Eq. 18 and Eq. 20 can differ by factors of the form  $(\text{const.})^{n_p}$  and  $(\text{const.})^V$  where  $(\text{const.})$  is any factor independent of  $V$  and  $n_p$ . Such factors have no physical consequence on phase equilibria since they only contribute as additive constants to the osmotic pressure and chemical potential, and will therefore always cancel in balance equations. The factors  $Z_{w,\psi}$  in Eq. 20 amount to such constant contributions to the osmotic pressure. Similarly, sources of constant contributions to  $\beta\mu$  include excluded-volume and electrostatic self-energies in  $\hat{H}_{1,2}$ , and the normalization factor  $(3/2\pi b^2)^{3(N-1)/2}$  in  $Q[\check{w}, \check{\psi}]$  (which is chosen for convenience to make  $Q[0, 0] = 1$ ).

Applying the definition of chemical potential in Eq. 37a to the field form of the partition



function in Eq. 20 leads to

$$\beta\mu = \ln \frac{n_p}{V} - \left\langle \ln Q[\check{w}, \check{\psi}] \right\rangle_{\text{F}}. \quad (38)$$

A direct application of Eq. 37b leads to an osmotic pressure operator that suffers from UV divergences. These divergences can be regulated by subtracting the contributions from  $Z_w Z_\psi$  (which can be calculated analytically since  $Z_w$  and  $Z_\psi$  are exactly solvable Gaussian integrals). However, a much more efficient approach exists where the factors  $Z_w Z_\psi$  are used to derive a regularized osmotic pressure operator that is manifestly insensitive to the fluctuations on scales  $\lesssim \bar{a}$  [78]. Before taking the volume derivative in Eq. 37b, we consider the rescaled coordinates  $\mathbf{z} = V^{-1/3}\mathbf{r}$  and write the functional integrals in terms of the rescaled fields  $w'(\mathbf{z}) = V^{1/2}w(\mathbf{r})$  and  $\psi'(\mathbf{z}) = V^{1/6}\psi(\mathbf{r})$ . In effect, this isolates the volume dependence to the single chain partition function  $Q[V^{-1/2}\check{w}', V^{-1/6}\check{\psi}']$ . Eq. 37b then leads to

$$\beta\Pi = \frac{n_p}{V} + \left\langle \frac{n_p}{Q[V^{-1/2}\check{w}', V^{-1/6}\check{\psi}']} \frac{\partial Q[V^{-1/2}\check{w}', V^{-1/6}\check{\psi}']}{\partial V} \right\rangle_{\text{F}}, \quad (39)$$

where the field average is understood to be taken with respect to  $w'$  and  $\psi'$ . After computing the volume derivative of the single chain partition function in Eq. 39, and returning to the original coordinates  $\mathbf{r}$  and field variables  $w$  and  $\psi$ , we obtain a regularized osmotic pressure operator as

$$\beta\Pi = \frac{n_p}{V} - \left\langle \frac{n_p}{V} \int \frac{d\mathbf{r}}{V} \left[ \frac{b^2}{9} \mathcal{P}_\nabla + \sum_{\alpha=1}^N \mathcal{P}_\alpha \left\{ i(\Gamma_2 - \frac{\Gamma}{2}) \star w + i\sigma_\alpha(\Gamma_2 - \frac{\Gamma}{6}) \star \psi \right\} \right] \right\rangle_{\text{F}}, \quad (40)$$

where  $\mathcal{P}_\nabla = Q^{-1} \sum_{\alpha=1}^N q_F(\mathbf{r}, \alpha) \nabla^2 \exp[iW(\mathbf{r}, \alpha)] q_B(\mathbf{r}, \alpha)$ ,  $\mathcal{P}_\alpha = Q^{-1} q_B(\mathbf{r}, \alpha) \exp[iW(\mathbf{r}, \alpha)] q_F(\mathbf{r}, \alpha)$ , and  $\Gamma_2(\mathbf{r}) = (1 - r^2/3\bar{a}^2)\Gamma(\mathbf{r})$  with Fourier transform  $\hat{\Gamma}_2(\mathbf{k}) = (a^2 k^2/3)\hat{\Gamma}(\mathbf{k})$ .

Figure 5 shows  $\beta\Pi(\rho)$  and  $\beta\mu(\rho)$  computed using the functions in the FTS code [https://github.com/jwessen/IDP\\_phase\\_separation/blob/main/FTS\\_polyampholytes.py](https://github.com/jwessen/IDP_phase_separation/blob/main/FTS_polyampholytes.py). For each bulk density  $\rho$ , a polymer solution object `PolySol` was created on an  $M = 32$  lattice with  $\Delta x = \bar{a} = b/\sqrt{6}$ ,  $v = 0.0068b^3$ ,  $l_B = 0.38b$  and charge sequence `sv20`. The model polyampholyte sequence `sv20` is one of the thirty overall neutral “sv” sequences in ref. [22]. Here we use several “sv” sequences as well as the `as1`, `as4` model polyampholyte sequences from ref. [30] as examples in Fig. 5 and some of the subsequent figures. The field variables, represented by  $w \rightarrow \mathbf{w}$  and  $\psi \rightarrow \mathbf{psi}$ , were initially set to random complex values using the `PolySol.set_fields` function. The fields were then evolved with time-step  $\Delta t = 0.01$  in CL time using the `CL_step_SI` function, which implements the semi-implicit integration scheme. At every 50th step, the polymer chemical potential  $\beta\mu$  and osmotic pressure  $\beta\Pi$  were computed using `PolySol.get_chem_pot()` and `PolySol.get_pressure()`. After an initial  $10^3$  steps, the thermal averages were computed during a period of  $4 \times 10^4$  steps. Upon plotting  $\beta\mu$  against  $\beta\Pi$ , we see that the resulting curve self-intersects, signalling phase

separation. The condensed and dilute bulk densities are then obtained by numerically finding the corresponding two densities of the self-intersection point. This procedure can then be repeated at several temperatures to obtain the binodal curve enclosing the co-existence region in a  $(\rho, T^*)$  phase diagram, where  $T^* = b/l_B$  is the reduced temperature. Figure 6 shows such phase diagrams in the  $(\rho, T^*)$  plane, computed for several model sequences. This method of computing the phase diagram gives the critical chemical potential and pressure as a by-product, which can be used to map the coexistence curve in  $(\beta\mu, T^*)$  and  $(\beta\Pi, T^*)$  phase diagrams, shown here in Fig. 7 for the sequences in Fig. 6a. To elucidate the relationship between FTS and approximate analytical formulations, the FTS results in Figs. 6 and 7 (filled circles) are contrasted with RPA predictions (solid line in Fig. 6 and dotted lines in Fig. 7) to be described below.

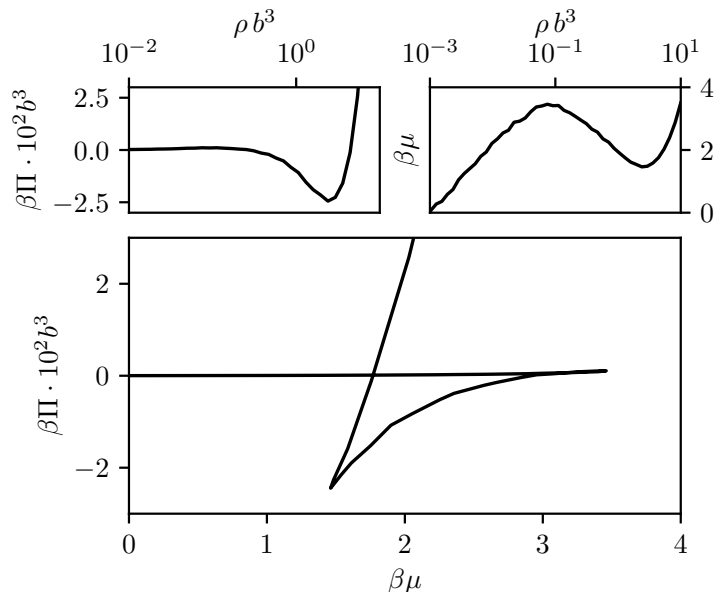


FIG. 5: Chemical potential  $\beta\mu$  and osmotic pressure  $\beta\Pi$  computed in FTS in a system of sv20 chains under phase separation conditions;  $v = 0.0068b^3$ ,  $l_B = 0.38b$ , and  $M = 32$ .

### 3.5 Random phase approximation (RPA)

As an alternative approach, for certain applications one may opt to sacrifice the high degree of accuracy of FTS in favor of numerical efficiency, in which case one can compute  $\beta\mu$  and  $\beta\Pi$  analytically by neglecting field fluctuations beyond quadratic order; i.e., by using the expanded field Hamiltonian in Eq. 31 instead of the full Hamiltonian in Eq. 21. This approach is known as the random phase approximation (RPA). In RPA, the functional integrals that appear in the partition function are Gaussian and therefore exactly solvable.

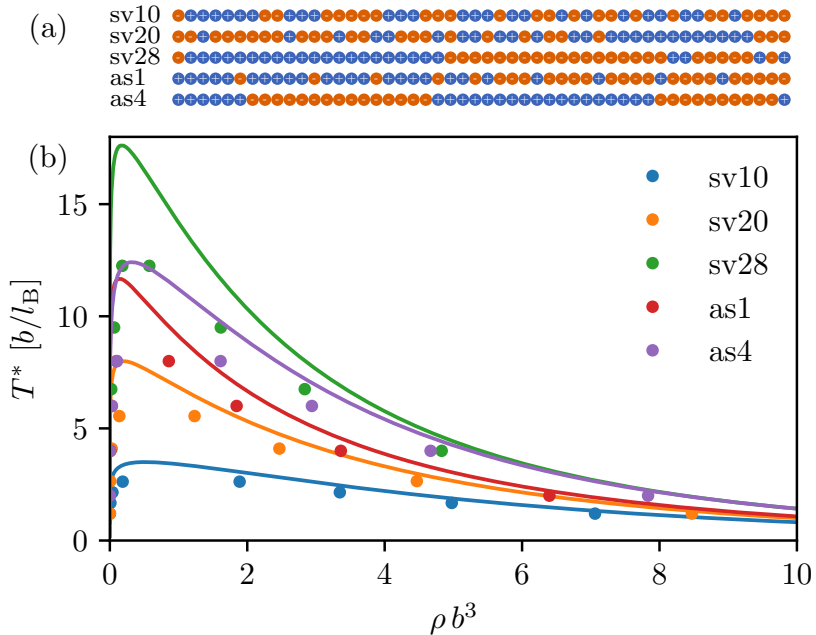


FIG. 6: Comparing FTS with RPA. (a) Model charge sequences considered in this work. Positively and negatively charged beads are depicted, respectively, in blue and red. (b)  $(\rho, T^*)$  phase diagrams computed in FTS (filled circles) and RPA (solid lines);  $v = 0.0068b^3$  and  $M = 32$  are used for FTS. The present results for sv10 and sv20 are consistent with the corresponding results in Fig. 3C of ref. [32].

For the present model, this leads to the following RPA free energy in units of  $k_B T$ :

$$-\ln Z = \ln n_p! - n_p \ln V + \frac{v(Nn_p)^2}{2V} + \frac{V}{2} \int \frac{d\mathbf{k}}{(2\pi)^3} \ln \left( \frac{4\pi l_B v}{k^2} \det \hat{\mathbf{K}} \right), \quad (41)$$

where the matrix  $\hat{\mathbf{K}}$  is given by Eq. 35 and the factor  $4\pi l_B v/k^2$  comes from  $Z_w Z_\psi$ . It is instructive to note that in the  $v \rightarrow 0$  limit, aside from the overall volume factor  $V$ , the last term in Eq. 41 for  $-\ln Z$  corresponds to the RPA electrostatic free energy  $f_{\text{el}}$  in Eq. 3 of ref. [17] in the absence of the subtraction of self-energy term  $\text{Tr}(\hat{\rho}\hat{U}_k)$  in this equation and the  $1/k^2 \rightarrow 1/k^2[1 + (ka)^2]$  in  $\hat{U}_k$  to implement a short spatial range cutoff of Coulomb interaction in ref. [17] (similar  $f_{\text{el}}$  are used in refs. [18, 19]). In other words, when the trace term is eliminated from  $f_{\text{el}}$  and  $1/k^2[1 + (ka)^2]$  in  $\hat{U}_k$  is reverted back to  $1/k^2$  in ref. [17], the last term in Eq. 41 is seen to be equal to  $Vf_{\text{el}}$ . This correspondence is consistent with the fact that excluded volume is accounted for by incompressibility in the RPA theory of ref. [17] but not by an explicit term in the Hamiltonian as in Eq. 41 and that UV divergences are regularized by the short spatial range cutoff of Coulomb interaction in ref. [17] rather than using the Gaussian smearing in Eq. 41.

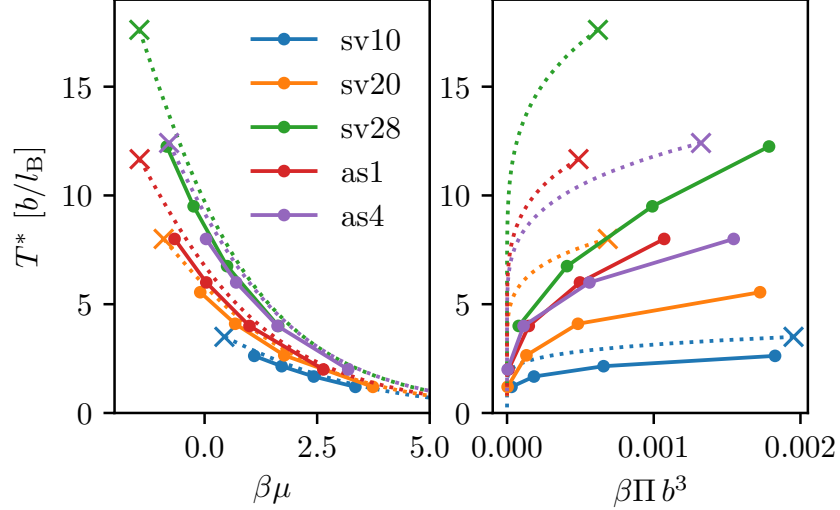


FIG. 7: Chemical potential and osmotic pressure of coexisting phases.  $(\beta\mu, T^*)$  and  $(\beta\Pi, T^*)$  phase diagrams, i.e.,  $\beta\mu(T^*)$  and  $\beta\Pi(T^*)$  of the coexisting phases, are computed using FTS (filled circles) and RPA (dotted lines) for the five model sequences in Fig. 6 (same color key). As in Fig. 6,  $v = 0.0068b^3$  and  $M = 32$  are used for FTS. Crosses indicate the position of the critical point estimated in RPA. Solid lines through the FTS data points are merely a guide for the eye.

Applying Stirling's approximation  $\ln n_p! \approx n_p \ln n_p - n_p$  to Eq. 41, the chemical potential and osmotic pressure in RPA become

$$\beta\mu = \ln \frac{\rho}{N} + vN\rho + \frac{N}{4\pi^2} \int_0^\infty dk k^2 \frac{A + 2B\rho}{1 + A\rho + B\rho^2}, \quad (42a)$$

$$\beta\Pi = \frac{\rho}{N} + \frac{v\rho^2}{2} + \frac{1}{4\pi^2} \int_0^\infty dk k^2 \left[ \frac{A\rho + 2B\rho^2}{1 + A\rho + B\rho^2} - \ln(1 + A\rho + B\rho^2) \right], \quad (42b)$$

where  $\rho \equiv n_p N/V$  is the polymer bead bulk density,  $A \equiv \hat{\Gamma}_k^2(vg_k^{\text{mm}} + 4\pi l_B g_k^{\text{cc}}/k^2)$  and  $B \equiv \hat{\Gamma}_k^4 4\pi l_B v(g_k^{\text{mm}} g_k^{\text{cc}} - g_k^{\text{mc}2})/k^2$ . Once the integrals over  $k$  have been performed numerically, phase separation is indicated by self-intersection points of the curve  $(\beta\Pi(\rho), \beta\mu(\rho))$ . Solid lines in Fig. 6 and dotted lines in Fig. 7 correspond to RPA phase diagrams computed in this way, using the RPA code available as [https://github.com/jwessen/IDP\\_phase\\_separation/blob/main/RPA\\_polyampholytes.py](https://github.com/jwessen/IDP_phase_separation/blob/main/RPA_polyampholytes.py). These figures show that RPA tends to overestimate the phase separation propensity, largely due to an overestimation of the dilute phase chemical potential.

### 3.6 Practical guide to codes for RPA and FTS with Figs. 5–7 as examples

We now conclude the preceding few sections on FTS by providing a guide to how the functions contained in the codes `RPA_polyampholytes.py`, `FTS_polyampholytes.py`, `FTS_trajectories_MPI.py`, and `FTS_analyze_trajectories.py` available from

[https://github.com/jwessen/IDP\\_phase\\_separation](https://github.com/jwessen/IDP_phase_separation) can be used to calculate phase diagrams in RPA and FTS for the polyampholyte solutions. More details can be found in the document

[https://github.com/jwessen/IDP\\_phase\\_separation/blob/main/rpa\\_fts\\_guide.pdf](https://github.com/jwessen/IDP_phase_separation/blob/main/rpa_fts_guide.pdf).

**3.6.1 RPA:** When executing `RPA_polyampholytes.py`, the script produces (i) a plot depicting the self-intersection behavior of the  $(\beta\mu(\rho), \beta\Pi(\rho))$  curve at an example value of  $l_B$ , and (ii) the full phase diagram (i.e. the binodal curve) in the  $(\rho, T^*)$ -plane, the latter corresponding to the RPA curves in Fig. 6. The RPA curves in Fig. 7 were generated by computing  $\beta\mu$  and  $\beta\Pi$  at the densities of the binodal curve using the `PolySol_RPA.calc_mu_Pi` function. Users may modify parameters in the `main` function to generate their own desired polyampholyte RPA phase diagrams. In particular, the charge sequence  $(\sigma_\alpha \rightarrow \text{seq})$  can be selected from sequences contained in `CL_seq_list.py`. Other model parameters are represented as  $v \rightarrow \mathbf{v}$ ,  $l_B \rightarrow \mathbf{lB}$  and  $\bar{a} \rightarrow \mathbf{a}$ .

**3.6.2 FTS:** The accompanying FTS code `FTS_polyampholytes.py` contains the definition of a `PolySol` object, representing a field picture description of a polyampholyte solution, which has methods necessary for computation of chemical potential  $\beta\mu$  and osmotic pressure  $\beta\Pi$  through CL evolution. Its `main` function, which is run upon the execution of the script, contains a usage example for generating the CL time trajectories  $\beta\mu(t)$  and  $\beta\Pi(t)$ .

The Python script `FTS_trajectories_MPI.py` may be used to calculate a phase diagram using a computer cluster where many cores are available. The script imports `FTS_polyampholytes.py` to calculate time trajectories  $\beta\mu(t)$  and  $\beta\Pi(t)$  at several densities, each trajectory is assigned to a separate CPU utilising the Python `multiprocessing` module. The resulting trajectory files can then be analyzed using the script `FTS_analyze_trajectories.py` that produces one file per temperature containing the  $(\rho, \beta\mu, \beta\Pi)$  data (e.g., those shown in Fig. 5) and then calculates the self-intersection points of the  $(\beta\mu(\rho), \beta\Pi(\rho))$  curves yielding the binodal curve. The reduced temperature ( $T^*$ ), the densities ( $\rho$ 's) of the co-existing phases, their osmotic pressures and chemical potentials are written to a file which can subsequently be used to plot FTS phase diagrams as in Fig. 6 ( $\rho$  vs  $T^*$ ) and Fig. 7 ( $\beta\mu$  vs  $T^*$  and  $\beta\Pi$  vs  $T^*$ ).

While our FTS method is well-suited for computer clusters since calculations at each  $\rho$  value can be performed in parallel, readers are encouraged to also explore a highly efficient Gibbs ensemble method that does not necessitate parallel computation [79].

### 3.7 Multicomponent systems

We have so far considered simple systems with only one polymer component. Formally, the above FTS method can be extended in a straightforward manner to systems with multiple components, such as mixtures of polymers with different charge sequences [25], or inclusions of explicit solvents and ions [35]. Restricting the interaction types to excluded volume and electrostatics while adding more components (labeled by  $p$ ) to the system modifies the canonical field Hamiltonian, with  $n_p \ln Q[\check{w}, \check{\psi}] \rightarrow \sum_q n_q \ln Q_q[\check{w}, \check{\psi}]$  wherein

the summation now runs over all components  $q$ ,  $Q_q$  is the partition function for a single unit of component  $q$ , and  $n_q$  is the number of molecules of component  $q$ .

Practically, the phase behaviour of multicomponent systems can be difficult to investigate because of the multiple chemical potentials that need to be matched at the phase boundary (see Sect. 2.3 above). Nevertheless, some structural information can be obtained from FTS of a phase-separated multicomponent system in the canonical ensemble by using density-density correlation functions, defined as [25]:

$$G_{p,q}(|\mathbf{r} - \mathbf{r}'|) = \langle \hat{\rho}_p(\mathbf{r}) \hat{\rho}_q(\mathbf{r}') \rangle, \quad (43)$$

where  $\hat{\rho}_p(\mathbf{r})$  is the microscopic density of component  $p$  (analogously to Eq. 17a). If the system is in a single-phase homogeneous fluid state, all correlation functions  $G_{p,q}(r)$  will approach the product of bulk densities  $\rho_p \rho_q$  at large  $r$ . An inhomogeneous state, on the contrary, will show nontrivial correlations at length scales comparable to the system size due to the inhomogeneous partitioning of the system components. For example, if the system contains a polymer-dense phase-separated droplet in a dilute surrounding, the polymer self-correlation function  $G_{p,p}(r)$ , with  $p$  serving as label for the component type, takes on large values at small  $r$  and decreases to  $\sim 0$  for  $r$  larger than the droplet size. Cross-correlation functions  $G_{p,q}(r)$  between the polymers and other components  $q$  can then reveal to what extent these components reside inside or outside the droplet.

The field operators corresponding to density-density correlation functions can be obtained by adding species-specific density source terms  $-\int d\mathbf{r} \hat{\rho}_q(\mathbf{r}) J_q(\mathbf{r})$  to the Hamiltonian before deriving the field theory. As is customary in field-theoretic analyses [80], functional derivatives of the partition function with respect to  $J_q(\mathbf{r})$  in the field theory, followed by setting all  $J_q$  to zero, then gives the desired field operators. Utilising an intermediate field re-definition (see ref. [25] for detailed derivation) gives the following convenient field representations of the correlation functions,

$$G_{p,q}(|\mathbf{r} - \mathbf{r}'|) = \langle \tilde{\rho}_p(\mathbf{r}) \tilde{\rho}_q(\mathbf{r}') \rangle_{\text{F}} \quad (p \neq q), \quad (44a)$$

$$G_{p,p}(|\mathbf{r} - \mathbf{r}'|) = \frac{i}{v} \langle w(\mathbf{r}) \tilde{\rho}_p(\mathbf{r}') \rangle_{\text{F}} - \sum_{q \neq p} \langle \tilde{\rho}_p(\mathbf{r}) \tilde{\rho}_q(\mathbf{r}') \rangle_{\text{F}}. \quad (44b)$$

As a demonstration of how the correlation functions could be used to extract information about the structural organization of multiple species in a phase separated droplet, here we perform FTS of two pairs of sequences, sv28–sv24 and sv28–sv9. For the results presented in this section, we used the same basic Python script for single-component FTS computations but generalized to include multiple charge sequences. A Github link for the script is [https://github.com/mmTanmoy/IDP\\_phase\\_separation/blob/main/FTS\\_polyampholytes\\_multi\\_species.py](https://github.com/mmTanmoy/IDP_phase_separation/blob/main/FTS_polyampholytes_multi_species.py). To ensure phase separation of all the individual sequences, we chose a small reduced temperature  $T^* = 0.2$  or, equivalently, a large Bjerrum length  $l_B = 5b$ . Other parameters for

the FTS are  $M = 32$ ,  $\Delta x = \bar{a} = b/\sqrt{6}$ ,  $\Delta t = 5 \times 10^{-4}$ , and  $v = 0.068b^3$ , and a common bulk bead density of  $0.2b^{-3}$  for both species of the pair of sequences. It is noteworthy that here we used a  $v$  value which is 10 times larger than the one used to calculate the phase diagrams in Figs. 6 and 7. As observed in ref. [25], a relatively large  $v$  value is necessary—albeit not sufficient by itself—for demixing of different polyampholyte species in the condensed phases, supporting the principle that both a significant sequence charge-pattern mismatch and a strong sequence-independent, generic excluded-volume repulsion are needed for membraneless organelle subcompartmentalization-like demixing of polyampholyte species in condensed droplets. For the results presented here, a total of 40 independent simulations were conducted for each parameter set and for each run, field configurations were sampled at an interval of  $500\Delta t$  for a total CL time  $3 \times 10^4\Delta t$  after discarding  $2 \times 10^4$  initial CL steps for equilibration.

The thermal-averaged correlation functions for the two pairs simulated are shown in Fig. 8. From the self-correlation function plots and the representative snapshots, formation of a single droplet is evident. Cross-correlation function plots demonstrate clear sequence dependence, in the sense that the cross-correlation function for the sv28–sv9 pair peaks at a lower value compared to the sv28–sv24 pair. This feature is interpreted as indicating that the sv28 and sv24 pair mixes more in the common droplet compared to sv28 and sv9 pair, as is evident from the snapshots in Fig. 8 showing sv28 population is more concentrated in the center of the droplet when it is paired with sv9, but is more diffused throughout the droplet when it is paired with sv24 [25]. The routines for computing different correlation function could be found through the link [https://github.com/mmTanmoy/IDP\\_phase\\_separation/blob/main/calc\\_correlations.py](https://github.com/mmTanmoy/IDP_phase_separation/blob/main/calc_correlations.py). In addition to the software referenced above, part of the software applicable to the FTS study of polyampholyte LLPS with explicit solvent [35] is available at [https://github.com/laphysique/FTS\\_polyampholyte\\_water](https://github.com/laphysique/FTS_polyampholyte_water). We emphasize, however, that the code currently shared on this webpage is only a prototype; thus it should be used with caution.

### 3.8 Practical guide to multicomponent FTS with Fig. 8 as an example

A step-by-step recipe for using the FTS codes for multicomponent LLPS in the [https://github.com/mmTanmoy/IDP\\_phase\\_separation](https://github.com/mmTanmoy/IDP_phase_separation) repository is as follows. First, running the scripts requires the Python3.x, Numpy, Pandas and Mayavi packages. After these packages are installed, download the FTS\_Canonical.tar.gz file from the above-cited Github repository and extract its content (untar the file). Among its content, the `submit_to_cluster.py` script contains the main function that runs the simulation by importing the `FTS_polyampholytes_multi_species.py` and `CL_seq_list.py` scripts. After choosing a charge sequence pair from `CL_seq_list.py`, `ncpus` copies of the `Polysol()` object (defined in `FTS_polyampholytes_multi_species.py`) are created and each will then be passed to the `exe` target function along with their unique run labels to be executed in

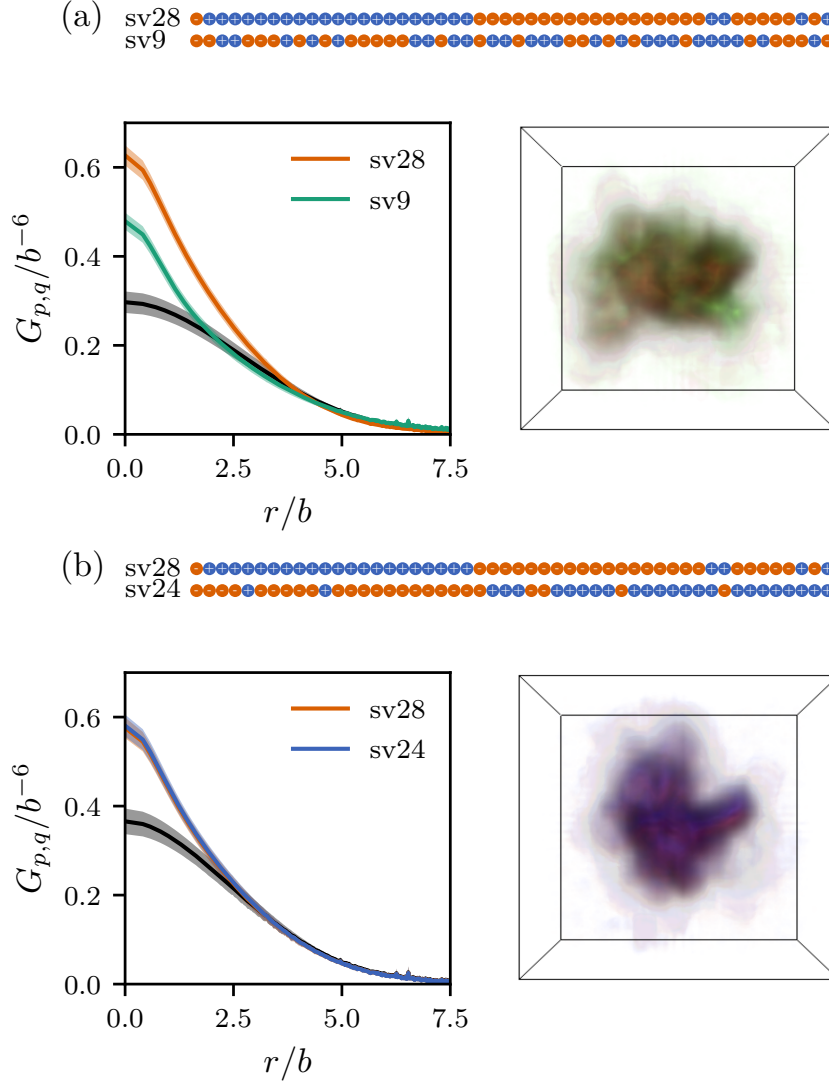


FIG. 8: FTS-computed density correlation and mixing/demixing of polyampholyte species in condensed droplets. Results are obtained using  $v = 0.068b^3$ ,  $l_B = 5b$ , and  $M = 32$ . (a) Top: The charge sequences of the sv28–sv9 pair (same color code as that in Fig. 6a). Lower-left: Solid black line is cross-correlation function ( $p \neq q$ ), and colored solid lines are self-correlation functions ( $p = q$ ) of individual sequences plotted using the color key shown in this panel. The solid lines and the shaded regions around the solid lines are, respectively, the mean and the extent of standard deviation of the correlation functions computed over 40 independent runs. Lower-right: Representative snapshot of the real positive parts of the bead-density operators  $\tilde{\rho}_{sv28}(\mathbf{r})$  and  $\tilde{\rho}_{sv9}(\mathbf{r})$  following the color key in the left panel. (b) Same as (a) but for the sv28–sv24 pair. In this case, the self-correlation functions of sv28 and sv24 essentially overlap. Data presented in this figure were generated using a Python script which is available freely on Github through the link [https://github.com/mmTanmoy/IDP\\_phase\\_separation/blob/main/FTS\\_polyampholytes\\_multi\\_species.py](https://github.com/mmTanmoy/IDP_phase_separation/blob/main/FTS_polyampholytes_multi_species.py).

parallel on ncpus CPUs. At this point, one can start executing the `submit_to_cluster.py`



script after setting the total CL time steps and the CL sampling interval (`n_cpus` is a variable in `submit_to_cluster.py`). The snapshots will be saved in the `densities` folder and the time evolution of the single chain partition functions ( $Q_s$ ) are saved in the `evolution` folder, both on the fly. One can observe CL time evolution of the  $Q_s$  to determine the CL time needed of equilibrium. Once equilibration is achieved, subsequent snapshots can be used as inputs to run the script `calc_correlations.py` that output a text file containing the means and the standard deviations of the pair distribution functions as a function of spatial distance  $r$ , which in turn can be used to compute correlation functions  $G_{p,q}(r)$  such as those shown along the left column of Fig. 8. The script `plot_snapshot.py` provided under [https://github.com/mmTanmoy/IDP\\_phase\\_separation](https://github.com/mmTanmoy/IDP_phase_separation) and also in the `visualization` folder of `FTS_Canonical.tar.gz` is for visualizing the bead-density profiles of phase separated droplets or absence thereof by using the generated snapshot files as inputs. As an example, the snapshot files for plotting the bead-density profile along the right column of Fig. 8 are also provided in the same folder for readers who wish to test run the codes.

## 4 Coarse-Grained Molecular Dynamics

Because structural details are lacking in analytical theories and FTS, it is desirable—and often necessary—to check their predictions against explicit-chain models that embody a higher degree of physico-chemical realism. However, it has been a computational challenge to apply conventional simulation techniques for the study of phase separation of Ising systems, relatively simple fluids, and homopolymer solutions [81–85] to biomolecular LLPS because of the large system size the latter entails, the large number of chain molecules it involves, and the need to account for heteropolymeric sequence dependence. Against this backdrop, a recently developed multiple-chain simulation protocol for coarse-grained explicit-chain IDP models emerges as an efficient methodology for simulating sequence-dependent IDP phase separation [36]. The key advantage of this approach is that it reduces the computational cost significantly by initiating the main simulation with a slab-like configuration of condensed polymers, leading to relatively fast equilibration of phase-separated states by Langevin molecular dynamics [37], although phase equilibrium can also be achieved by simulations of similar coarse-grained IDP chain models without using the slab-like initial state [36, 86]. Since 2018, the “slab” methodology has been applied to study phase behaviors of the FUS [36, 87], LAF-1 [34, 36], and Ddx4 [34] IDRs, IDP-RNA mixtures [88], IDPs in an explicit model of water [89], model polyampholytes [30], mixtures of two polyampholyte species with different sequence charge patterns [25], as well as model polyampholytes in simple dipole solvent molecules [35].

In our implementation of this simulation protocol, we have used the GPU-based HOOMD-blue package [90, 91] version 2.5.1, which is fast computationally and user-friendly (<http://glotzerlab.engin.umich.edu/hoomd-blue/>).

As the main purpose of this chapter is to serve as a practical guide to numerical techniques

for analytical formulations, our brief review of explicit-chain modeling of biomolecular LLPS is limited to this “slab” approach. Other explicit-chain simulation software packages the reader may also wish to consult—but are beyond the scope of this chapter—include the LAMMPS materials modeling package [92] (<https://lammps.sandia.gov/>) and the recently developed lattice-based LASSI package tailored specifically to biomolecular LLPS [42] (<https://bio.tools/LASSI>).

#### 4.1 A coarse-grained explicit-chain model of IDPs

As described originally in ref. [36] for the “slab” approach, each amino acid residue is modeled as a single spherical bead, with differences in mass, electrical charge, size, and interactions to account for the differences among the residues. The potential energy consists of bond, non-bonded short-range, and electrostatic interaction terms. Bond-angle energies for two consecutive bonds and torsional energies for three consecutive bonds can be included but usually not considered. The bond-length terms are harmonic potentials, with reference bond length set to the *trans* C<sub>α</sub>–C<sub>α</sub> distance of 3.8 Å. Currently, the non-bonded interactions are mostly modeled by either the HPS [93, 94] or the KH [95, 96] potential (energy matrix) between pairs of amino acid residues, which can be readily implemented using a small python script in HOOMD-blue. Strengths and limitations of the HPS and KH potentials with respect to their abilities to capture hydrophobicity and  $\pi$ -related interactions have recently been assessed by applying these potentials to variants of the Ddx4 and LAF-1 IDRs [34]. In addition to the interactions in the HPS and KH potentials, other interaction types such as cation- $\pi$  can be incorporated [34]. Hydrophobicity scales, other than HPS, that are more suitable for IDP simulations have also been proposed recently [97, 98]. Electrostatics is tackled by the PPPM module [99] in the HOOMD-blue package, which has the option to include screening length to account approximately for the effects of salt. If the difference in salt concentration between the dilute and condensed phases is of interest, it is also straightforward to model salt ions explicitly. Details of the coarse-grained interaction schemes and their biophysical implications can be found in refs. [34] and [36].

The coarse-grained nature of the model allows us to use a relatively long time step of 10 fs for Langevin dynamics simulations. Periodic boundary conditions are usually applied to all three spatial dimensions. To enhance computational efficiency, we use a cut-off distance of 15 Å for non-bonded interactions. It should be noted that HOOMD-blue uses reduced units. Hence, one needs to convert common physical units to reduced units before starting a simulation. This conversion process is described in the section on units in the HOOMD-blue package. An exposition that uses an actual simulation system as example is also available in ref. [99].

#### 4.2 An efficient protocol for simulating polymer LLPS

In the “slab” protocol for simulating polymer LLPS [37], all the polymers (IDPs in our case) are initially inserted randomly in a sufficiently large cubic box. Typically, one to sev-

eral hundred IDP chains are used. For this initial preparation step, the Packmol package [100] (<http://leandro.iqm.unicamp.br/m3g/packmol/home.shtml>) or HOOMD-blue’s own module for building initial configurations can be used. The system is then energy minimized to remove steric clashes among molecules using the FIRE algorithm provided in the HOOMD-blue package. A few hundred ps of simulation run is usually sufficient for this energy minimization step. It is advisable, however, to monitor the fluctuations in potential energy, temperature, and other thermodynamic properties during the course of the simulations to ensure that the run is proceeding properly. Once stability of the system is ascertained, *NPT* simulations are performed for approximately 50 ns to compress the simulation box at a sufficient lower temperature, e.g., at 100 K. A low temperature is chosen for this compression process to produce a high-IDP-density configurational state for the next step of the simulation protocol. The Martyna-Tobias-Klein (MTK) thermostat and barostat [101, 102] provided in the HOOMD-blue package may be used for this *NPT* simulation. Alternatively, one may also use the `update.box.resize` module to compress the box. However, as it is not known a priori how much compression would be sufficient to produce a desirable high-density state, *NPT* followed by box-resizing is a better option per our experience. In this connection, it should be noted that this *NPT* simulation step is merely a computational technique to achieve a high-IDP-density state. When explicit solvent is absent, the pressure applied to the simulation box is not equivalent to the physical hydrostatic pressure experienced by the corresponding real-world IDP solution system.

The compressed box is then expanded symmetrically along the direction of one of the box edges (referred to as the  $z$ -axis) by using the `update.box.resize` module at a sufficiently low temperature. During the expansion process, molecules are unwrapped only in the  $z$ -direction because the periodic boundary conditions in the  $x$  and  $y$  directions remain unchanged. The expansion process results in a slab of condensed IDPs in the middle of the elongated simulation box. The system is then equilibrated by Langevin dynamics at the temperature of interest for  $2 \mu\text{s}$ . The production run is finally carried out for another  $\sim 4 \mu\text{s}$ . In our experience [34] and that of others [36], an overall  $6\text{-}\mu\text{s}$  simulation run is usually sufficient for simulating the phase behavior at one given temperature when the system contains  $\sim 100$  IDP chains and each chain is consisting of a few hundred amino acid residues. Recognizing that the friction coefficient in Langevin dynamics affects kinetic but not equilibrated thermodynamic properties, weak friction coefficients are used in these simulations to accelerate configurational sampling for the computation of phase diagrams.

For systems in which model IDPs are simulated with explicit solvents [35], an equilibrated system comprising only of the IDPs is first prepared in accordance with the above procedure. The solvent molecules are then inserted into the simulation box using either one’s own script or the Packmol package [100]. During the insertion process, suitable distance criteria should be maintained to avoid steric overlaps. After inserting the solvent molecules, the system is equilibrated again before commencement of the production run.

### 4.3 Construction of phase diagrams from simulation data

The coexistence curve (phase diagram) of a system with a single IDP species is constructed by first computing at different temperatures the distributions of IDP population in the simulation box under the constraint that the center of mass is fixed at  $z = 0$ . At a given temperature, the distribution is determined by dividing the simulation box into many small bins along the  $z$ -axis and tallying IDP density in each bin. An example of this procedure is provided in Fig. 9. At sufficiently high temperatures (weak interaction strengths), the density is essentially uniform throughout the box as the system is in a homogeneous state (Fig. 9a). At sufficiently low temperatures (strong interaction strengths), a region of maximum density appears around  $z = 0$  with much lower densities in the other parts of the simulation box, indicating phase separation (Fig. 9c). These two different densities can then be mapped onto two points on the coexistence curve for the given temperature (Fig. 9b). After repeating this procedure for several temperatures, the critical temperature may be estimated. Following ref. [37], the critical temperature,  $T_{\text{cr}}$ , and the critical density,  $\rho_{\text{cr}}$ , are estimated using the scaling laws

$$\frac{\rho_{\text{cond}}(T) + \rho_{\text{dil}}(T)}{2} = \rho_{\text{cr}} + A(T_{\text{cr}} - T) , \quad (45)$$

$$\rho_{\text{cond}}(T) - \rho_{\text{dil}}(T) = B(1 - T/T_{\text{cr}})^{\nu} , \quad (46)$$

where  $\rho_{\text{cond}}(T)$  and  $\rho_{\text{dil}}(T)$  are, respectively, condensed and dilute phase density at temperature  $T$ ,  $A$  and  $B$  are fitting parameters, and  $\nu$  is a critical exponent set to 0.325 [37] based on the three-dimensional Ising model universality class [103]. The red coexistence curve in Fig. 9b is produced by this fitting procedure. As further illustrations of the simulated phase behaviors of the model LAF-1 system in Fig. 9, snapshots of simulated configurations generated by the VMD package [104, 105] (<https://www.ks.uiuc.edu/Research/vmd/>) are provided in Fig. 9d and f.

Additional snapshots generated using the same package are provided in Fig. 10 to illustrate two recent applications of the “slab” simulation protocol: Figure 10a–e shows condensed-phase demixing of two polyampholyte species with significantly different sequence charge patterns, supporting predictions by RPA [24] and FTS [25] (see also Fig. 8). Figure 10f–j shows a polyampholyte-rich droplet in explicit solvent as observed in a recent study of dielectric effects in polyampholyte condensates [35].

### 4.4 Practical guide to using the “slab” protocol to simulate biomolecular LLPS

The protocol begins with the generation of the initial configuration of the system. This task can be accomplished efficiently by Packmol [100], which offers a variety of input and output file formats. The input script is user friendly and available from the website (see Sect. 4.2 above). After successful compilation of the initial configuration, the python input script of the HOOMD-blue package is utilized for running the

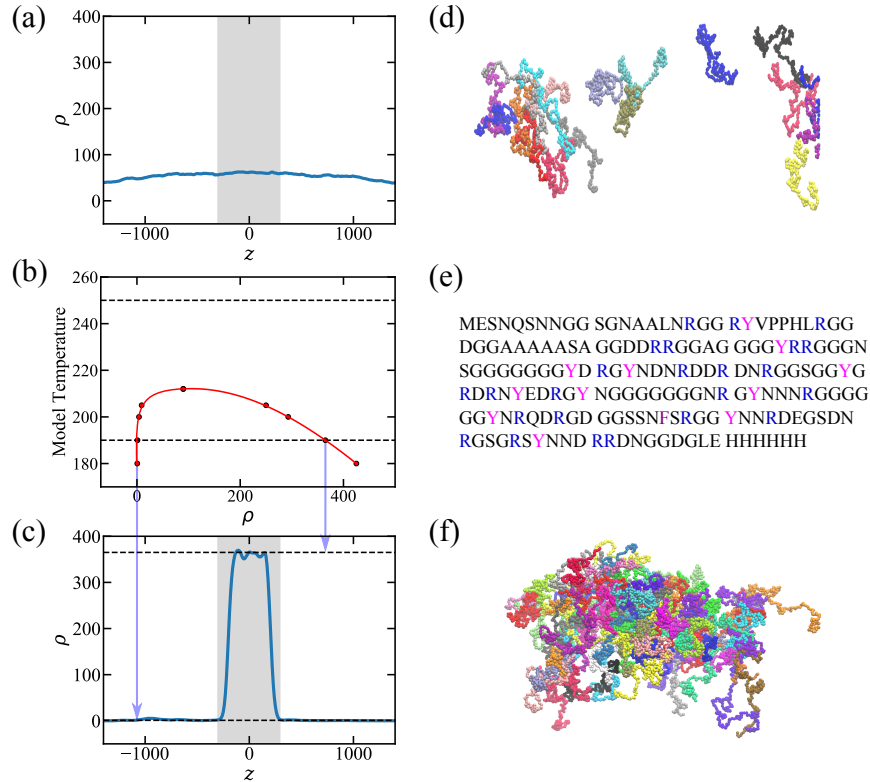


FIG. 9: Coarse-grained explicit-chain simulation of heteropolymer phase behaviors. Results shown are for the wildtype LAF-1 RGG IDR model studied in ref. [34]. As described in this reference, simulation is conducted by the “slab” protocol using 100 chains with the KH interaction scheme [36, 96] and a uniform dielectric constant  $\epsilon_r = 40$ . (a) Polymer (IDR) density profile ( $\rho$ , in units of mg/ml) at a temperature indicated by the upper horizontal dashed line in (b), which is higher than the critical temperature of the model system. The blue curve gives the density distribution along the  $z$  dimension of the simulation box ( $z$  is in units of Å). (b) Phase diagram constructed from simulated data points (red circles). All data points except the ones at model temperature = 205 are from ref. [34]. The critical point is estimated by the procedure described in the text. The red curve is an empirical fit. (c) Density profile at a lower temperature indicated by the lower horizontal dashed line in (b). Phase separation is indicated by a polymer droplet with elevated  $\rho$  in the shaded region. The light blue vertical arrows from (b) to (c) show how the points on the coexistence curve in (b) at a given temperature are obtained from the  $\rho$  values in the dilute and condensed parts of the density profile at that temperature. (d) A snapshot of the shaded region in (a) showing polymer chains in a homogeneous solution. Chains are colored differently to enhance visualization of their individual configurations. (e) Sequence of the LAF-1 RGG IDR studied, given by the one-letter code for the amino acids. As in ref. [34], positively charged arginine and aromatic tyrosine and phenylalanine residues are shown in blue, magenta, and deep purple, respectively, to highlight the pattern of their positions along the sequence. (f) A snapshot of the shaded region in (c) showing a condensed droplet; chains at the boundaries of the periodic simulation box are unwrapped in this depiction.

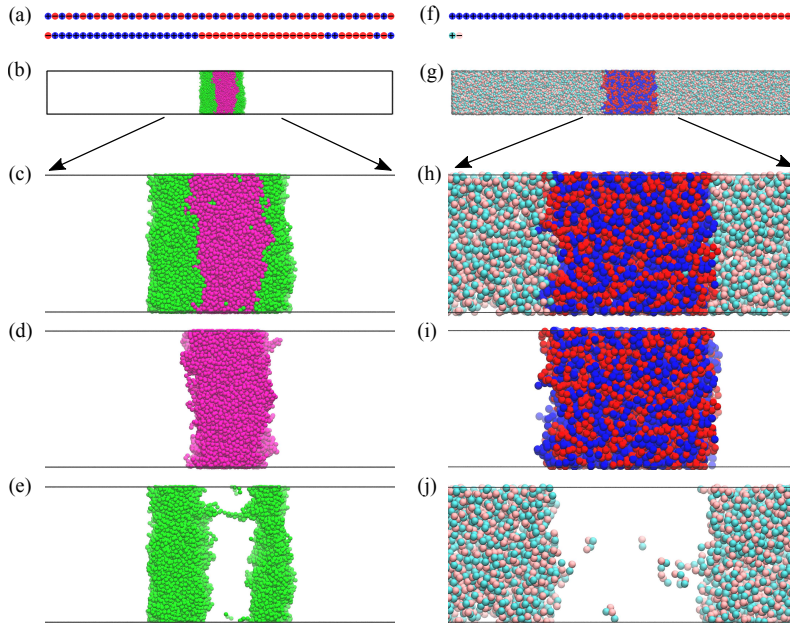


FIG. 10: Condensed-phase demixing of polyampholytes and LLPS effects of explicit polar solvent. Snapshots from coarse-grained explicit-chain simulations using the “slab” protocol. (a)–(e): A two-polyampholyte system consisting of sequences sv1 and sv28 described in ref. [25]. (a) sv1 (upper) and sv28 (lower), shown in the style of Fig. 6a. (b) A snapshot of the equilibrated simulation box at reduced temperature  $T^* = 0.6$ ; sv1 and sv28 chains are depicted, respectively, in green and magenta. (c)–(e): Zoomed-in view of the condensed droplet. The separate depictions of sv28 (d) and sv1 (e) underscore that the two sequence populations are largely demixed in the condensed phase. (f)–(j): A system consisting of sv30 chains and dipole solvent molecules as described in ref. [35]. (f) sv30 (upper, same style as (a)) and the dipole solvent molecule, for which the positively and negatively charged beads are depicted in cyan and pink respectively. (g) A snapshot of part of the equilibrated simulation box at reduced temperature  $T^* = 3.0$ , with charges  $q_d = \pm 3.888$  on each dipole. The color scheme of the sv30 chains and the dipoles is the same as that in (f) to highlight the positions of opposite charges in the system. (h)–(j): Zoomed-in view of the condensed droplet. The separate depictions of sv30 (i) and dipole (j) indicate that some dipole solvent molecules are present inside the polymer-rich condensed droplet.

simulations. Readers who are not familiar with the input scripts for HOOMD-blue may first consult the examples in the tutorial section of the HOOMD-blue website. However, while the examples on the HOOMD-blue website convey a clear idea about how to simulate simple Lennard-Jones polymers, simulations of biomolecular LLPS often require more complex input scripts, a good example of the latter is available at [https://bitbucket.org/jeeain/hoomd\\_slab\\_builder/src/master/](https://bitbucket.org/jeeain/hoomd_slab_builder/src/master/), which provides the input codes for simulating FUS condensates [93]. Schematically, the entire “slab” protocol may be recapitulated as follows: (i) Initial configuration generated from other sources such as Packmol + HOOMD-blue input script  $\rightarrow$  (ii) Energy minimization  $\rightarrow$  (iii)  $NPT$  box compression  $\rightarrow$  (iv) Box expansion along  $z$  axis  $\rightarrow$  (v) Box equilibration

→ (vi) Final production run → (vii) Number density calculation + other analyses → (viii) Construction of phase diagram.

## 5 Concluding Remarks

In summary, we have provided a brief summary of the formulations for several analytical theories and a practical guide to general numerical techniques that are useful for extracting LLPS information from these theories in the form of two-component (one polymer solute) and three-component (two polymer solutes) phase diagrams by determining the pertinent spinodal regions and coexisting (binodal) conditions, using data from FH and rG-RPA theories as examples. With links to corresponding software, we have also presented algorithms for performing CL sampling in FTS, which relies quite heavily on analytical formulation and involves considerable computation, but is valuable for modeling sequence-dependent LLPS without invoking some of the approximations in analytical theories such as RPA. In addition, an efficient simulation protocol for a class of coarse-grained explicit-chain models of biomolecular LLPS is briefly outlined as well. The versatile methodology is important in its own right and also as a model with relatively more physical realism to compare against predictions by abstract analytical approaches such as FH, RPA, rG-RPA, and FTS. While we have covered only a fraction of the theoretical/computational approaches to biomolecular condensates, it is our hope that as a practical guide, this chapter would be useful for researchers in the field, especially those who have not begun but wish to initiate theoretical investigations. Despite considerable advances made in the past few years, theoretical/computational investigation of biomolecular condensates is still in its early stages of development. It will take many complementary methodologies to decipher the physical basis of the myriad biological functions that are being discovered by the rapidly expanding experimental effort on biomolecular condensates.

### Acknowledgments

This work was supported by Canadian Institutes of Health Research grant NJT-155930 and Natural Sciences and Engineering Research Council of Canada grant RGPIN-2018-04351 as well as computational resources provided generously by Compute/Calcul Canada to H.S.C.

Y.-H.L., J.W., and T.P. contributed equally to this work.

## References

---

- [1] Banani SF, Lee HO, Hyman AA, Rosen MK (2017) Biomolecular condensates: organizers of cellular biochemistry. *Nat Rev Mol Cell Biol* 18:285–298
- [2] Hyman AA, Weber CA, Jülicher F (2014) Liquid-liquid phase separation in biology. *Annu Rev Cell Dev Biol* 30:39–58
- [3] Brangwynne CP, Tompa P, Pappu RV (2015) Polymer physics of intracellular phase transitions. *Nat Phys* 11:899–904
- [4] Shin Y, Brangwynne CP (2017) Liquid phase condensation in cell physiology and disease. *Science* 357:eaaf4382
- [5] Boeynaems S, Alberti S, Fawzi NL, Mittag T, Polymenidou M, Rousseau F, Schymkowitz J, Shorter J, Wolozin B, Van Den Bosch L, Tompa P, Fuxreiter M (2018) Protein phase separation: a new phase in cell biology. *Trends Cell Biol* 28:420–435
- [6] McSwiggen DT, Mir M, Darzacq X, Tjian R (2019) Evaluating phase separation in live cells: diagnosis, caveats, and functional consequences. *Genes Dev* 33:1619–1634
- [7] Weber CA, Zwicker D, Jülicher F, Lee CF (2019) Physics of active emulsions. *Rep Prog Phys* 82:064601
- [8] Kato M, Han TW, Xie S, Shi K, Du X, Wu LC, Mirzaei H, Goldsmith EJ, Longgood J, Pei J, Grishin NV, Frantz DE, Schneider JW, Chen S, Li L, Sawaya MR, Eisenberg D, Tycko R, McKnight SL (2012) Cell-free formation of RNA granules: low complexity sequence domains form dynamic fibers within hydrogels. *Cell* 149:753–767
- [9] Nott TJ, Petsalaki E, Farber P, Jervis D, Fussner E, Plochowietz A, Craggs TD, Bazett-Jones DP, Pawson T, Forman-Kay JD, Baldwin AJ (2015) Phase transition of a disordered nuage protein generates environmentally responsive membraneless organelles. *Mol Cell* 57:936–947
- [10] Lin Y-H, Forman-Kay JD, Chan HS (2018) Theories for sequence-dependent phase behaviors of biomolecular condensates. *Biochemistry* 57:2499–2508
- [11] Cinar H, Fetahaj Z, Cinar S, Vernon RM, Chan HS, Winter R (2019) Temperature, hydrostatic pressure, and osmolyte effects on liquid-liquid phase separation in protein condensates: Physical chemistry and biological implications. *Chem Eur J* 57:13049–13069
- [12] Flory PJ (1953) *Principles of Polymer Chemistry*. Cornell University Press, Ithaca, NY.
- [13] Overbeek JTG, Voorn MJ (1957) Phase separation in polyelectrolyte solutions. Theory of complex coacervation. *J Cell Comp Physiol* 49:7–26
- [14] Rauscher S, Pomès R (2017) The liquid structure of elastin. *eLife* 6:e26526
- [15] Zheng W, Dignon GL, Jovic N, Xu X, Regy RM, Fawzi NL, Kim YC, Best RB, Mittal J (2020) Molecular details of protein condensates probed by microsecond long atomistic simulations. *J Phys Chem B* 124:11671–11679



- [16] Ermoshkin AV, Olvera de la Cruz M (2003) A modified random phase approximation of polyelectrolyte solutions. *Macromolecules* 36:7824–7832
- [17] Lin Y-H, Forman-Kay JD, Chan HS (2016) Sequence-specific polyampholyte phase separation in membraneless organelles. *Phys Rev Lett* 117:178101
- [18] Lin Y-H, Song J, Forman-Kay JD, Chan HS (2017) Random-phase-approximation theory for sequence-dependent, biologically functional liquid-liquid phase separation of intrinsically disordered proteins. *J Mol Liq* 228:176–193
- [19] Lin Y-H, Chan HS (2017) Phase separation and single-chain compactness of charged disordered proteins are strongly correlated. *Biophys J* 112:2043–2046
- [20] Amin AN, Lin Y-H, Das S, Chan HS (2020) Analytical theory for sequence-specific binary fuzzy complexes of charged intrinsically disordered proteins. *J Phys Chem B* 124:6709–6720
- [21] Dignon GL, Zheng W, Best RB, Kim YC, Mittal J (2018) Relation between single-molecule properties and phase behavior of intrinsically disordered proteins. *Proc Natl Acad Sci USA* 115:9929–9934
- [22] Das RK, Pappu RV (2013) Conformations of intrinsically disordered proteins are influenced by linear sequence distributions of oppositely charged residues. *Proc Natl Acad Sci USA* 110:13392–13397
- [23] Sawle L, Ghosh K (2015) A theoretical method to compute sequence dependent configurational properties in charged polymers and proteins. *J Chem Phys* 143:085101
- [24] Lin Y-H, Brady JP, Forman-Kay JD, Chan HS (2017) Charge pattern matching as a ‘fuzzy’ mode of molecular recognition for the functional phase separations of intrinsically disordered proteins. *New J Phys* 19:115003
- [25] Pal T, Wessén J, Das S, Chan HS (2021) Subcompartmentalization of polyampholyte species in organelle-like condensates is promoted by charge-pattern mismatch and strong excluded-volume interaction. *Phys Rev E* 103:042406
- [26] Feric M, Vaidya N, Harmon TS, Mitrea DM, Zhu L, Richardson TM, Kriwacki RW, Pappu RV, Brangwynne CP (2016) Coexisting liquid phases underlie nucleolar subcompartments. *Cell* 165:1686–1697
- [27] Lafontaine DLJ, Riback JA, Bascetin R, Brangwynne CP (2021) The nucleolus as a multi-phase liquid condensate. *Nat Rev Mol Cell Biol* 22:165–182
- [28] Lin Y-H, Brady JP, Chan HS, Ghosh K (2020) A unified analytical theory of heteropolymers for sequence-specific phase behaviors of polyelectrolytes and polyampholytes. *J Chem Phys* 152:045102
- [29] Das S, Eisen A, Lin Y-H, Chan HS (2018) A lattice model of charge-pattern-dependent polyampholyte phase separation. *J Phys Chem B* 122:5418–5431
- [30] Das S, Amin AN, Lin Y-H, Chan HS (2018) Coarse-grained residue-based models of disordered protein condensates: Utility and limitations of simple charge pattern parameters. *Phys Chem Chem Phys* 20:28558–28574
- [31] Fredrickson GH (2006) *The Equilibrium Theory of Inhomogeneous Polymers*. Oxford Uni-

- versity Press, New York, NY.
- [32] McCarty J, Delaney KT, Danielsen SPO, Fredrickson GH, Shea J-E (2019) Complete phase diagram for liquid-liquid phase separation of intrinsically disordered proteins. *J Phys Chem Lett* 10:1644–1652
  - [33] Danielsen SPO, McCarty J, Shea J-E, Delaney KT, Fredrickson GH (2019) Molecular design of self-coacervation phenomena in block polyampholytes. *Proc Natl Acad Sci USA* 116:8224–8232
  - [34] Das S, Lin Y-H, Vernon RM, Forman-Kay JD, Chan HS (2020) Comparative roles of charge,  $\pi$ , and hydrophobic interactions in sequence-dependent phase separation of intrinsically disordered proteins. *Proc Natl Acad Sci U S A* 117:28795–28805
  - [35] Wessén J, Pal T, Das S, Lin Y-H, Chan HS (2021) A simple explicit-solvent model of polyampholyte phase behaviors and its ramifications for dielectric effects in biomolecular condensates. *J Phys Chem B* 125:4337–4358
  - [36] Dignon GL, Zheng W, Kim YC, Best RB, Mittal J (2018) Sequence determinants of protein phase behavior from a coarse-grained model. *PLoS Comput Biol* 14:e1005941
  - [37] Silmore KS, Howard MP, Panagiotopoulos AZ (2017) Vapour–liquid phase equilibrium and surface tension of fully flexible Lennard–Jones chains. *Mol Phys* 115:320–327
  - [38] Schuster BS, Dignon GL, Tang WS, Kelley FM, Ranganath AK, Jahnke CN, Simplins AG, Regy RM, Hammer DA, Good MC, Mittal J (2020) Identifying sequence perturbations to an intrinsically disordered protein that determine its phase separation behavior. *Proc Natl Acad Sci USA* 117:11421–11431
  - [39] Vernon RM, Chong PA, Tsang B, Kim TH, Bah A, Farber P, Lin H, Forman-Kay JD (2018) Pi-Pi contacts are an overlooked protein feature relevant to phase separation. *eLife* 7:e31486
  - [40] Song J, Ng SC, Tompa P, Lee KAW, Chan HS (2013) Polycation- $\pi$  interactions are a driving force for molecular recognition by an intrinsically disordered oncoprotein family. *PLoS Comput Biol* 9:e1003239
  - [41] Chen T, Song J, Chan HS (2015) Theoretical perspectives on nonnative interactions and intrinsic disorder in protein folding and binding. *Curr Opin Struct Biol* 30:32–42
  - [42] Choi J-M, Dar F, Pappu RV (2019) LASSI: A lattice model for simulating phase transitions of multivalent proteins. *PLoS Comput Biol* 15:e1007028
  - [43] Nilsson D, Irbäck A (2020) Finite-size scaling analysis of protein droplet formation. *Phys Rev E* 101:022413
  - [44] Robichaud NAS, Saika-Voivod I, Wallin S (2019) Phase behavior of blocky charge lattice polymers: Crystals, liquids, sheets, filaments, and clusters. *Phys Rev E* 100:052404
  - [45] Nguemaha V, Zhou H-X (2018) Liquid-liquid phase separation of patchy particles illuminates diverse effects of regulatory components on protein droplet formation. *Sci Rep* 8:6728
  - [46] Espinosa JR, Joseph JA, Sanchez-Burgos I, Garaizar A, Frenkel D, Collepardo-Guevara R (2020) Liquid network connectivity regulates the stability and composition of biomolecular condensates with many components. *Proc Natl Acad Sci USA* 117:13238–13247.

- [47] Sing CE (2017) Development of the modern theory of polymeric complex coacervation. *Adv Coll Interface Sci* 239:2–16
- [48] Sing CE, Perry SL (2020) Recent progress in the science of complex coacervation. *Soft Matter* 16:2885–2914
- [49] Semenov AN, Rubinstein M (1998) Thermoreversible gelation in solutions of associative polymers. 1. Statics. *Macromolecules* 31:1373–1385
- [50] Bawendi MG, Freed KF, Mohanty U (1987) A lattice field theory for polymer systems with nearest-neighbor interaction energies. *J Chem Phys* 87:5534–5540
- [51] Baker D, Chan HS, Dill KA (1993) Coordinate-space formulation of polymer lattice cluster theory. *J Chem Phys* 98:9951–9962
- [52] Wertheim MS (1986) Fluids with highly directional attractive forces. IV. Equilibrium polymerization. *J Stat Phys* 42:477–492
- [53] Kastelic M, Kalyuzhnyi YV, Vlachy V (2016) Modeling phase transitions in mixtures of  $\beta$ - $\gamma$  lens crystallins. *Soft Matter* 12:7289–7298
- [54] Shen K, Wang Z-G (2017) Electrostatic correlations and the polyelectrolyte self energy. *J Chem Phys* 146:084901
- [55] Nelder JA, Mead R (1965) A simplex method for function minimization. *Comput J* 7:308–313
- [56] Fletcher R (1987) *Practical Methods of Optimization*. John Wiley & Sons Ltd., New York, NY.
- [57] Cinar H, Oliva R, Lin Y-H, Chen X, Zhang M, Chan HS, Winter R (2020) Pressure sensitivity of SynGAP/PSD-95 condensates as a model for postsynaptic densities and its biophysical and neurological ramifications. *Chem Eur J* 26:11024–11031
- [58] Lin Y-H, Wu H, Jia B, Zhang M, Chan HS (2022) Assembly of model postsynaptic densities involves interactions auxiliary to stoichiometric binding. *Biophys J* 121:157–171
- [59] Dill KA, Alonso DOV, Hutchinson K (1989) Thermal stabilities of globular proteins. *Biochemistry* 28:5439–5449
- [60] Dignon GL, Zheng W, Kim YC, Mittal J (2019) Temperature-controlled liquid-liquid phase separation of disordered proteins. *ACS Cent Sci* 5:821–830
- [61] Jacobs WM, Frenkel D (2017) Phase transitions in biological systems with many components. *Biophys J* 112:683–691
- [62] Broyden CG (1965) A class of methods for solving nonlinear simultaneous equations. *Math Comput* 19:577–593
- [63] Press WH, Teukolsky SA, Vetterling WT, Flannery BP (2007) *Numerical Recipes: The Art of Scientific Computing* (3rd ed). Cambridge University Press, New York, NY, p 509 [Section 10.7. Direction set (Powell’s) methods in multidimensions]
- [64] Byrd RH, Lu P, Nocedal J, Zhu C (1995) A limited memory algorithm for bound constrained optimization. *SIAM J Sci Comput* 16:1190–1208
- [65] Kraft D (1988) *A Software Package for Sequential Quadratic Programming*. Deutsche Forschungs- und Versuchsanstalt für Luft- und Raumfahrt Forschungsbericht (DFVLR Re-

- port). Wiss. Berichtswesen d. DFVLR, Köln (Cologne), Germany.
- [66] Lin Y, McCarty J, Rauch JN, Delaney KT, Kosik KS, Fredrickson GH, Shea J-E, Han S (2019) Narrow equilibrium window for complex coacervation of tau and RNA under cellular conditions. *eLife* 8:e42571
  - [67] Matsen MW (2006) Self-consistent field theory and its applications. In: Gompper G, Schick M (eds) *Soft Matter: Polymer Melts and Mixtures*. Wiley-VCH, Weinheim, Germany. pp 87–178
  - [68] Wang Z-G (2010) Fluctuation in electrolyte solutions: The self energy. *Phys Rev E* 81:021501
  - [69] Edwards SF (1965) The statistical mechanics of polymers with excluded volume. *Proc Phys Soc* 85:613–624
  - [70] Fredrickson GH, Ganesan V, Drolet F (2002) Field-theoretic computer simulation methods for polymers and complex fluids. *Macromolecules* 35:16–39
  - [71] Parisi G (1983) On complex probabilities. *Phys Lett B* 131:393–395
  - [72] Klauder JR (1983) A Langevin approach to fermion and quantum spin correlation functions. *J Phys A: Math Gen* 16:L317–L319
  - [73] Parisi G, Wu Y-S (1981) Perturbation theory without gauge fixing. *Sci Sin* 24:483–496
  - [74] Chan HS, Halpern MB (1986) New ghost-free infrared-soft gauges. *Phys Rev D* 33:540–547
  - [75] Damgaard PH, Hüffek H (1987) Stochastic quantization. *Phys Rep* 152:227–398
  - [76] Lennon EM, Mohler GO, Ceniceros HD, García-Cervera CJ, Fredrickson GH (2008) Numerical solutions of the complex Langevin equations in polymer field theory. *Multiscale Model Sim* 6:1347–1370
  - [77] Kardar M (2007) *Statistical Physics of Particles*. Cambridge University Press, New York, NY.
  - [78] Villet MC, Fredrickson GH (2014) Efficient field-theoretic simulation of polymer solutions. *J Chem Phys* 141:224115
  - [79] Riggleman RA, Fredrickson GH (2010) Field-theoretic simulations in the Gibbs ensemble. *J Chem Phys* 132:024104
  - [80] Itzykson C, Zuber J-B (1980) *Quantum Field Theory*. McGraw-Hill Inc., New York, NY.
  - [81] Panagiotopoulos AZ (1992) Direct determination of fluid phase equilibria by simulation in the Gibbs ensemble: A review. *Mol Simul* 9:1–23
  - [82] Binder K (1985) The Monte Carlo method for the study of phase transitions: A review of some recent progress. *J Comput Phys* 59:1–55
  - [83] Panagiotopoulos AZ (1987) Direct determination of phase coexistence properties of fluids by Monte Carlo simulation in a new ensemble. *Mol Phys* 61:813–826
  - [84] Panagiotopoulos AZ, Quirke N, Stapleton M, Tildesley DJ (1988) Phase equilibria by simulation in the Gibbs ensemble. *Mol Phys* 63:527–545
  - [85] Panagiotopoulos AZ (2000) Monte Carlo methods for phase equilibria of fluids. *J Phys Condens Matter* 12:R25–R52.
  - [86] Hazra MK, Levy Y (2020) Charge pattern affects the structure and dynamics of polyam-

- polyte condensates. *Phys Chem Chem Phys* 22:19368–19375.
- [87] Murthy AC, Dignon GL, Kan Y, Zerze GH, Parekh SH, Mittal J, Fawzi NL (2019) Molecular interactions underlying liquid-liquid phase separation of the FUS low-complexity domain. *Nat Struct Mol Biol* 26:637–648
- [88] Regy RM, Dignon GL, Zheng W, Kim YC, Mittal J (2020) Sequence dependent phase separation of protein-polynucleotide mixtures elucidated using molecular simulations. *Nucl Acids Res* 48:12593–12603
- [89] Zheng W, Dignon GL, Jovic N, Xu X, Regy RM, Fawzi NL, Kim YC, Best, RB, Mittal J (2020) Molecular details of protein condensates probed by microsecond long atomistic simulations. *J Phys Chem B* 124:11671–11679
- [90] Anderson JA, Glaser J, Glotzer SC (2020) HOOMD-blue: A Python package for high-performance molecular dynamics and hard particle Monte Carlo simulations. *Comput Mater Sci* 173:109363
- [91] Glaser J, Nguyen TD, Anderson JA, Lui P, Spiga F, Millan JA, Morse DC, Glotzer SC (2015) Strong scaling of general-purpose molecular dynamics simulations on GPUs. *Comput Phys Comm* 192:97–107
- [92] Plimpton S (1995) Fast parallel algorithms for short-range molecular dynamics. *J Comp Phys* 117:1–19
- [93] Regy RM, Zheng W, Mittal J (2021) Using a sequence-specific coarse-grained model for studying protein liquid-liquid phase separation. *Methods Enzymol* 646:1–17
- [94] Kapcha LH, Rossky PJ (2014) A simple atomic-level hydrophobicity scale reveals protein interfacial structure. *J Mol Biol* 426:484–498
- [95] Miyazawa S, Jernigan RL (1996) Residue-residue potentials with a favorable contact pair term and an unfavorable high packing density term, for simulation and threading. *J Mol Biol* 256:623–644
- [96] Kim YC, Hummer G (2008) Coarse-grained models for simulations of multiprotein complexes: Application to ubiquitin binding. *J Mol Biol* 375:1416–1433
- [97] Regy RM, Thompson J, Kim YC, Mittal J (2021) Improved coarse-grained model for studying sequence dependent phase separation of disordered proteins. *Protein Sci* 30:1371–1379.
- [98] Dannenhoffer-Lafage T, Best RB (2021) A data-driven hydrophobicity scale for predicting liquid-liquid phase separation of proteins. *J Phys Chem B* 125:4046–4056.
- [99] LeBard DN, Levine BG, Mertmann P, Barr SA, Jusufi A, Sanders S, Klein ML, Panagiotopoulos AZ (2012) Self-assembly of coarse-grained ionic surfactants accelerated by graphics processing units. *Soft Matter* 8:2385–2397
- [100] Martínez L, Andrade R, Birgin EG, Martínez JM (2009) PACKMOL: A package for building initial configurations for molecular dynamics simulations. *J Comput Chem* 30:2157–2164
- [101] Martyna GJ, Tobias DJ, Klein ML (1994) Constant pressure molecular dynamics algorithms. *J Chem Phys* 101:4177–4189
- [102] Tuckerman ME, Alejandre J, López-Rendón R, Jochim AL, Martyna GJ (2006) A Liouville-

- operator derived measure-preserving integrator for molecular dynamics simulations in the isothermal–isobaric ensemble. *J Phys A: Math Gen* 39:5629–5651
- [103] Rowlinson JS, Widom B (2002) *Molecular Theory of Capillarity*. Dover Publications, Mineola, NY
- [104] Humphrey W, Dalke A, Schulten K (1996) VMD - Visual Molecular Dynamics. *J Molec Graphics* 14:33–38
- [105] Hsin J, Arkhipov A, Yin Y, Stone JE, Schulten K (2008) Using VMD: an introductory tutorial. *Curr Protoc Bioinform* 24:5.7.1-5.7.48